Spatial variability of Saharan dust deposition revealed through a citizen science campaign

Marie Dumont[1,⋆], Simon Gascoin[2,⋆], Marion Réveillet[1,6], Didier Voisin[6], François Tuzet[1], Laurent Arnaud[6], Mylène Bonnefoy[8], Montse Bacardit Peñarroya[15], Carlo Carmagnola[1], Alexandre Deguine[9,10], Aurélie Diacre[14], Lukas Dürr[7], Olivier Evrard[3], Firmin Fontaine[8], Amaury Frankl[12,13], Mathieu Fructus[1], Laure Gandois[4], Isabelle Gouttevin[1], Abdelfateh Gherab[6], Pascal Hagenmuller[1], Sophia Hansson[4], Hervé Herbin[9], Béatrice Josse[5], Bruno Jourdain[6], Irene Lefevre[3], Gaël Le Roux[4], Quentin Libois[5], Lucie Liger[11], Samuel Morin[5], Denis Petitprez[10], Alvaro Robledano[6,1], Martin Schneebeli[7], Pascal Salze[11], Delphine Six[6], Emmanuel Thibert[8], Jürg Trachsel[7], Matthieu Vernay[1], Léo Viallon-Galinier[1], and Céline Voiron[6]

[1] Univ. Grenoble Alpes, Université de Toulouse, Météo-France, CNRS, CNRM, Centre d'Études de la Neige, 38000 Grenoble, France

[2] CESBIO, Université de Toulouse, CNES/CNRS/INRA/IRD/UPS, Toulouse, France

[3] LSCE- IPSL - Laboratoire des Sciences du Climat et de l'Environnement [Gif-sur-Yvette] , CEA, CNRS, UVSQ, Université Paris-Saclay, France

[4] Laboratoire Ecologie Fonctionnelle et Environnement, Université de Toulouse, CNRS, INPT, UPS, Toulouse, France

[5] CNRM, Université de Toulouse, Météo-France, CNRS, Toulouse, France

[6] Université Grenoble Alpes, CNRS, IRD, G-INP, IGE, Grenoble, France

[7] WSL Institute for Snow and Avalanche Research SLF, Flüelastr. 11, 7260 Davos, Switzerland

[8] Université Grenoble Alpes, INRAE, UR ETGR, Grenoble, France

[9] Université de Lille, CNRS, UMR 8518 - LOA - Laboratoire d'Optique Atmosphérique, F-59000 Lille, France

[10] Université de Lille, CNRS, UMR 8522 - PC2A - Physicochimie des Processus de Combustion et de l'Atmosphère, F-59000 Lille, France

[11] Jardin du Lautaret, CNRS, Université Grenoble Alpes, Grenoble, France

[12] INRAE, AMAP, IRD, CIRAD, CNRS, University Montpellier, Bld de la Lironde, 34398, Montpellier cedex 5, France

[13] Ghent University, Department of Geography, Krijgslaan 281 (S8), 9000, Ghent, Belgium

[14] Commissariat À L'Energie Atomique Et aux Énergies Alternatives (CEA, DAM, DIF), 91297 Arpajon, France

[15] Centre de Lauegi d'Aran, Conselh Generau d'Aran, Spain

⋆ Equal contribution

Correspondence: marie.dumont@meteo.fr

Abstract. Saharan dust outbreaks have profound effects on ecosystems, climate, human health and the cryosphere in Europe. However, the spatial deposition pattern of Saharan dust is poorly known due to a sparse network of ground measurements. Following the extreme dust deposition event of February 2021 across Europe, a citizen science campaign was launched to sample dust on snow over the Pyrenees and the European Alps. This somewhat improvised campaign triggered wide interest since 152 samples were collected in the snow in the Pyrenees, the French Alps and the Swiss Alps in less than four weeks. ~~An~~ Among the 152 samples, 113 in total could be analyzed, corresponding to 70 different locations. The analysis of the samples showed a large variability in the dust properties and amount. We found a decrease in the deposited mass and particle sizes with distance from the source along the transport path. This spatial trend was also evident in the elemental composition of the dust

as the iron mass fraction decreased from 11% in the Pyrenees to 2% in the Swiss Alps. At the local scale, we found a higher dust mass on south facing slopes, in agreement with estimates from high-resolution remote sensing data. This unique dataset, which resulted from the collaboration of several research laboratories and citizens, is provided as an open dataset to benefit a large community and enable further scientific investigations.

1 Introduction

Aeolian dust from the Sahara has a wide range of impacts on the Earth and society. For instance, airborne Saharan dust particles affect the Earth's radiative budget, cloud formation, solar energy production, and air traffic (Rieger et al., 2017; Varga, 2020; Ginoux, 2017; Nickovic et al., 2021) and could also impact human health (Tobías and Stafoggia, 2020). Once deposited, Saharan dust particles also provide nutrients to marine, aquatic and terrestrial ecosystems (Okin et al., 2004; Yu et al., 2015). Mountain regions are especially affected by the deposition of Saharan dust through several physical processes. Dust deposited on snow and ice modifies microbial abundance and diversity (Greilinger and Kasper-Giebl, 2021). Dust is also responsible for a darkening of snow- and ice-covered surfaces, which enhances the melting rates, leading to earlier meltwater runoff and the exposition of bare soil to the atmosphere (e.g. Skiles et al., 2018; He and He, 2022; Réveillet et al., 2022). Despite the episodic nature of dust outbreaks, a single event can have a major impact on snow cover duration. For instance, the dust deposition event that occurred in March 2018 over Eastern Europe led to a shortening of the snow cover duration by 12 to 30 days (Dumont et al., 2020). Such an effect strongly depends on the deposited dust mass and the dust optical properties (Réveillet et al., 2022).

While dust characteristics are well monitored at a few specific sites, little is known about the spatial variability of dust deposition, especially in complex mountain terrains where measurements are scarce (Baladima et al., 2022; Pey et al., 2020). The physico-chemical and optical properties of the dust particles are generally considered spatially homogeneous (Mărmureanu et al., 2019; Di Biagio et al., 2019). The mass of dust used in impact studies often originates from atmospheric models and is subject to significant uncertainties (Skiles and Painter, 2019). Indeed, dust deposition fluxes can differ by several orders of magnitude between models (Tuzet et al., 2019; Baladima et al., 2022). Finally, methods to estimate dust content on snow cover from satellite imagery are based on strong assumptions regarding the optical properties of dust particles, which are rarely supported by field data (Dumont et al., 2020) and are known to vary widely with the dust source region (Caponi et al., 2017; Skiles et al., 2018; He and He, 2022; Di Biagio et al., 2019).

In February 2021 (4 to 8 February and 18 to 25 February), two major Saharan dust outbreaks affected a large stretch of western Europe, turning the sky and the snow cover orange (Francis et al., 2022). Both events were associated with atmospheric rivers (Francis et al., 2022). The mass of dust deposited at the surface and the aerosol optical depth exceeded two standard deviations from the mean observed between 1980 and 2020 (Varga, 2020; Francis et al., 2022). The first event (4-8 February) was especially strong in terms of dust deposition in southern Europe and was widely reported in the media (see video supplement). The second event (18-25 February) transported dust as far as Scandinavia. Because these events occurred in winter, they represented a unique opportunity to study this phenomenon beyond conventional measurement networks. Indeed, the snow cover retained most of the dust particles and thus contained valuable information on the mass and type of the deposited dust

even weeks after deposition (Tuzet et al., 2019). All this prompted us to organise a citizen science campaign to collect dust samples across the European Alps and the Pyrenees. The campaign was launched the day after the publication of the first photographs of orange snow in social media and lasted four weeks. The samples resulting from the first deposition event were analysed to determine the mass, size distribution, chemical composition and optical properties of the dust. Several french news websites stated that the dust plume carried radionuclides from former french nuclear weapons tests in the Sahara. We thus also performed radionuclides analysis on the samples to verify this claim. This study presents the citizen science campaign and the results of the sample analysis.

2 Data and Methods

2.1 Citizen campaign

We initiated a citizen science campaign to collect samples of the "orange snow" on 6 February 2021, i.e., a day after the widespread deposition of orange dust on snow in the Pyrenees and the Alps. The sampling protocol was designed to be as simple as possible (Fig. 1). We asked participants to collect a snow sample of 10×10 cm^2 area (or any known area) up to the depth of the entire dust layer and to report the location of the sampling site. We recommended to take a photograph of the sampling site with a smartphone to obtain the coordinates of the sampling site. The call was first posted on social media (Twitter, YouTube, Facebook) and quickly relayed by traditional media, mostly local newspapers, TV and radio. Some people brought the samples directly to us in Toulouse or Grenoble; otherwise, we went to collect them. In any case, the snow was melted before reaching the laboratory.

2.2 Meteorological conditions

To characterise the meteorological conditions during the 4-8 February 2021 deposition event, we used simulations from the atmospheric transport model MOCAGE (Josse et al., 2004) and SAFRAN meteorological reanalysis (Vernay et al., 2022). Deposition and meteorological conditions were analysed at three sites: Pic du Midi (42.84°N, -0.44°E) in the Pyrenees, Queyras (44.74°N, 6.82°E) in the southern Alps and Chartreuse (45.29°N, 6.77°E) in the northern Alps. The dust load values were obtained using hourly dust deposition from MOCAGE. Dry and wet depositions were redistributed according to precipitation from the SAFRAN reanalysis. We further evaluated the accuracy of the total dust mass deposition from MOCAGE by comparison with the average averaged mass measured of the three closest samples for each site(see Sect. 2.3). . For the Chartreuse and Queyras locations the three samples are within the grid size resolution of MOCAGE (i.e. 10 km). For the Pyrenees, samples are located 60 to 70 km away and results might be taken with more caution. The three samples taken for each location covered different slope aspects. The three samples close to Pic du Midi also exhibit a larger spread in mass values that the samples for the two other locations.

1) Prélevez l'intégralité de la couche de neige orange
2) Prendre une photo avec un smartphone (géolocalisé)
3) Stockez chez vous (pas besoin de garder au frais)
4) Notez le diamètre de votre récipient de prélèvement
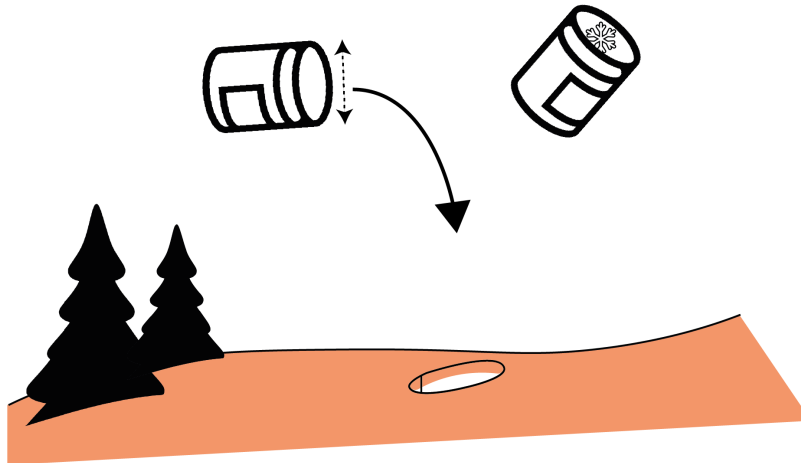
Figure 1. Original picture of the sampling protocol as posted on Twitter (in French). Translation in English: 1) Sample the whole layer of orange snow 2) Take a picture with a smartphone (geolocalised) 3) Store the sample at home (no need to keep it cool) 4) Write down the diameter of the container

2.3 Dust mass and size distribution

First, the samples were homogenised, and 5 mL of each sample was kept for size distribution analysis. The rest of the sample was ~~then filtered , dried, and weighed~~ vacuum filtered on 47 mm diameter pre-weighted polycarbonate membranes (pore size 0.45 μm), resulting in a $\approx$12.5 cm^2 loaded area. Those membranes were then dried in a dessicator, and weighted to provide the ~~dust concentration~~filtered dust mass. The analytical uncertainty of the measured dust mass is well within 5% (lower than 2% for 80% of samples). The dust surface concentration then results from dividing the measured mass by the snow sampled area, for which the uncertainty was not formally determined, so that 5% is a lower estimate of the overall uncertainty on that measurement.

Dust size distributions were measured with a Coulter counter ~~following Delmonte et al. (2004). This instrument counts and measures the size of insoluble particles above 0.6~~ (multisizer IIe) following protocols adapted from Delmonte et al. (2004). The main adaptation concerns the measured size range, which was set to $4 - 120$ μm by choosing a 200 μm measuring aperture. However, above $\approx$40-60 μm, depending on the sample's concentration, the size distributions measured with the Coulter counter ~~are hampered by~~ suffer from poor counting statistics~~above a certain size (example shown in Fig. 2)~~, as shown in Figure 2. We thus ~~separated the distribution in~~ determined for each sample a so-called cutoff diameter, as the lowest diameter where no particle was detected in any of the three individual replicate measurements (See Fig. 2 for an example). This cutoff diameter
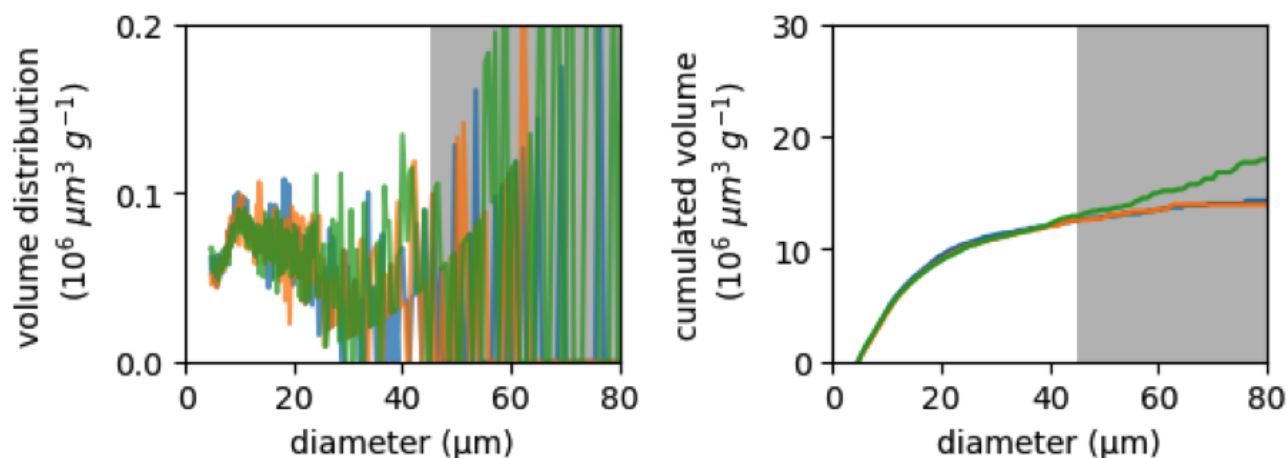
Figure 2. Volume size distributions measured by the Coulter counter for a sample. Panel (A): differential distribution. Panel (B): cumulative distribution. The shaded area shows the poorly constrained part of the distribution, yet it may represent a significant part of the total volume. The three lines correspond to three measurements for this sample.

(see Fig. S4 for values distribution) separates a lower part ~~, usually~~ of the distribution, well measured (typically better than 10% uncertainty), and ~~the tailof the distribution~~a tail, which is highly uncertain ~~,~~although it may represent a significant ~~fraction of the total mass~~ portion of the measured distribution (Fig. 2). ~~For each sample, we performed three measurements with the Coulter counter. The cut diameter between both parts of the distribution was estimated as the lowest diameter where none of~~
90 ~~the three individual measurements detected any particle.~~

2.4 Elemental composition

Before the analysis of the elemental composition, a picture of the dried filters was taken using a Universal Serial Bus (USB) microscope for a visual inspection of the filters and the detection of potential contamination with anthropogenic fibres such as microplastic fibres from the clothes of the person in charge of the sampling. The elemental composition of the filters was
95 determined using an X-ray fluorescence (XRF) analyser (ThermoFisher Scientific™ Niton™ XL3t). The direct analysis of the filters, with relatively thin dust layers (mass loads from 0.001 to 0.3 g), required the development of a specific calibration procedure provided with the dataset (see Data availability). Standard reference materials, including loess soil RTH 912 and Saharan dust samples, were analysed both after the deposition of a thin layer on a filter and using the standard cup of the XRF analyser. Using these paired measurements, a calibration function was developed by regression for every element between
100 the instrumental calibration for powdered rock measurements in the cup against the measurements of thin layers in filters. Satisfactory results were obtained for Al, Ca, K, Ti, Fe, P, Mn, Si, Rb, As, Pb, V, Cu and Sr. The calibration function is provided along with the dataset. However, most of the concentrations were below the quantification limits for Rb, As, Pb, V,

and Cu. In addition, we also calculated the Si/Al and Fe/Ca ratios and the mass fraction of Fe since these values were used in previous studies to determine the source region of the dust (Caponi et al., 2017).

2.5 Optical properties

For the analysis of optical properties, two specific samples were taken to ensure that a sufficient dust mass was available. We took two additional samples at a similar elevation of 2100 m near Pic du Midi de Bigorre in the Pyrenees and Col du Lautaret in the Alps.

The experimental setup used is extensively described by Hubert et al. (2017), and only a summary of the method is provided hereafter. A few tens of milligrams of dust were introduced into a vessel glass in which continuous mechanical agitation was maintained using a magnetic stirrer. By means of a continuous flow ($\approx$ 2 L min^{-1}) of pure nitrogen, particles were carried through the multipass cell of a Fourier transform infrared spectrometer (ThermoFisher Scientific™ iS50) to record the extinction spectra in the spectral range of 650-4000 cm^{-1} with a resolution of 1 cm^{-1}. To measure the size distribution of the particles over a larger range than that measured using the Coulter analyser, the flow was split into two parts at the exit of the infrared cell: one part was directed to a scanning mobility particle sizer (TSI™ 3936L75), which measures the particle number concentration as a function of the electric mobility diameter from 14.6 to 661 nm (64 bins/decade), and the second part was directed to an aerodynamic particle sizer (TSI™ 3321), which measures the particle number concentration as a function of the aerodynamic diameter from 0.542 to 20 μm (32 bins/decade). The size distributions of the two samples of interest are reported in Fig. S1, assuming that the electric mobility diameter is equal to the geometric diameter (d_g) and converting the aerodynamic diameter (d_a) measured by the aerodynamic particle sizer into d_g using Eq. 1 (DeCarlo et al., 2004):

$$d_g = d_a \sqrt{\frac{\chi \rho_0}{\rho_p}} \qquad (1)$$

where d_g and d_a are the geometric and aerodynamic diameters, respectively, χ is the dynamic shape factor (we assume $\chi \approx 1$), ρ_0 is the standard density of water (1 g cm^{-3}) and the mean density of Saharan particles, ρ_p = 2.7 g cm^{-3} (Schladitz et al., 2009). Then, each experimental size distribution was adjusted by a unimodal log-normal distribution whose number concentration, mean diameter and geometric standard deviation are N = 8800 cm^{-3}, $\overline{d_g}$= 0.37 μm and σ_g= 1.71 for the Lautaret sample and N = 3680 cm^{-3}, $\overline{d_g}$= 0.42 μm and σ_g= 1.77 for the Pic du Midi sample. These parameters are associated with the particle size distributions of dust travelling in the cell and not those of the bulk sample for which the coarse particles (typically > 3 μm, see section 2.3) are not resuspended in our experiment or are quickly deposited following sedimentation.

After purging the whole setup with pure nitrogen, the extinction spectrum in the infrared domain, $\Gamma_{sample} = -\log \frac{I(\tilde{\nu})}{I_0(\tilde{\nu})}$ was recorded, where $I(\tilde{\nu})$ and $I_0(\tilde{\nu})$ are the signals recorded with and without particles, respectively.

The mass extinction efficiency (MEE, in m^2 g^{-1}) at a given wavenumber, $\tilde{\nu}$, is defined as the ratio of the particles' light extinction coefficient (b_{ext} in m^{-1}) and the mass concentration, c in g m^{-3}, of the particles:

$$MEE(\tilde{\nu}) = \frac{b_{ext(\tilde{\nu})}}{c} \qquad (2)$$

where b_{ext} was calculated as the ratio of the measured extinction spectrum Γ_{sample} and the optical path length (10 m in this study).

2.6 Radionuclide analyses

~~Some of the filters~~ The filters with the highest dust load (ca. 0.1-0.3 g) were analysed using ultralow background Germanium HyperPure gamma spectrometry detectors installed in the underground facilities at University Paris-Saclay (Gif-sur-Yvette) and Modane (Underground Lab of Modane, France). To obtain sufficient counting statistics, filters were analysed for ca. $2x10^5$ s, approximately two days. The results obtained on the most heavily loaded filter (ALP-34-FE; 0.3 g of dust) and those obtained on a filter prepared with a similar quantity (0.3 g) of IAEA-444 soil-certified material were compared. All results were expressed in Bq kg^{-1} with activities decay-corrected to the sampling date. In addition to artificial ^{137}Cs (detected at 662 keV), natural fallout radionuclide activities (i.e., ^{7}Be at 477 keV and ^{210}Pb at 46 keV) were also quantified. ^{210}Pbb$_{xs}$ activities (representing the atmospheric fraction of ^{210}Pb alone) were calculated by subtracting the supported activity (determined using two ^{226}Ra daughters, ^{214}Pb (average count number at 295.2 and 351.9 keV) and ^{214}Bi (609.3 keV)) from the total ^{210}Pb activity.

To obtain larger quantities of radionuclide fallout, we performed two specific samplings in regions with significant deposition levels in ~~spring~~ early March 2021 (i.e., in addition to the samples from the citizen science campaign~~)~~., Tab. 1). The samples consist of dust from the two dust episodes that took place in February 2021. Initially, we sampled dust layers at the surface of snow cover randomly, but this yielded too little material (< 1 g per 20 L of snow). Therefore, we specifically collected dust that accumulated in the hollows that formed at the surface of snow cover by meltwater runoff. To select suitable sampling locations, we closely investigated the surface of snow patches and excluded areas where autochthonous sediment (i.e., produced within the catchment from runoff, mass movements, etc.) was present, as this would contaminate the allochthonous dust from the Sahara. This sampling was performed during the late snowmelt period (May 22-31, 2021) from two snow patches (locations: 42.903119 °N, 0.122031°E and 42.902679°N, 0.137037°E, Barèges, Pyrenees, France). Dust was collected using a shovel and stored in a fridge box for transportation. In the laboratory, the snow was melted in the spring sun, and clear water was poured off after the dust settled on the bottom of the refrigerator box. The remaining water was boiled until the dust was dry. We needed approximately 60 L of snow to collect 13 g of dust. This sample was prepared in a standard container for gamma spectrometry and analysed similarly for ^{137}Cs, ^{7}Be and ^{210}Pb as for the abovementioned filters. As sufficient quantity was available for this later sample, it was also analysed for plutonium contents and isotopic ratios (^{239}Pu, ^{240}Pu, ^{241}Pu, ^{242}Pu) at CEA, Arpajon, France, after radiochemical preparation and MC-ICP-MS measurements following all the methods detailed in Evrard et al. (2014) to gain additional insights into the potential sources of these radionuclides, given the public debate raised regarding the origin of ^{137}Cs and potentially the other artificial radionuclides found in the dust (Berger, 2021).

2.7 Satellite data

A multispectral image was captured by Sentinel-2B on 6 February 2021 at 10:49 UTC over the Pyrenees, i.e., the morning just after the dust deposition. In this image, we selected the only clear-sky area of 1150 km^2 spanning the snow-covered massifs

of Tabe and Vicdessos. Then, we selected the same region in the Sentinel-2A image that was captured five days later on 11 February 2021 (Figure 3). We chose this image because fresh snowfall occurred between the two dates. This allowed us to consider the 11 February image as a reference to remove the effect of the topography on the reflectance of the 6 February image (as done by Dumont et al., 2020). This "terrain normalisation" was performed using band 3 (green), and the dust content (dust concentration in ppm) was computed using band 8 (near infrared) following Eq. 1 in Dumont et al. (2020).

We performed this analysis with level-2A surface reflectance products processed with the MAJA atmospheric correction and cloud screening software (Hagolle et al., 2015, 2017). We used the snow maps derived from the same Sentinel-2 images to exclude from the analysis the pixels that were not covered by snow in both images (data available from Gascoin et al., 2019). These snow maps were computed at a spatial resolution of 20 m and then resampled to 10 m with the nearest neighbour method to match the resolution of band 3 and 8.

We studied the spatial variability of the resulting satellite-derived dust content, grouping the pixel values by topographic aspect classes to compare it with the spatial distribution obtained from the in situ samples.

The dust concentration retrievals from Sentinel-2 were computed in terms of mass fraction (mass mixing ratio, Flanner et al., 2021), whereas the analysis of the samples provided the total dust mass per unit area. To compare the same physical quantity between satellite retrievals and in situ samples, the snow density and the vertical profile of dust concentration should be known. In the absence of field observations, the estimation of such parameters would require additional modelling work, which is outside the scope of this article. Therefore, we limited our analysis to the comparison of the spatial variability of the dust concentrations from Sentinel-2 with the dust mass from the in situ samples.

3 Results

3.1 Citizen campaign

In total, in less than four weeks, 152 samples were collected: 84 in the French Alps, 9 in the Jura Mountains (France), 1 in the Massif Central (France), 26 in the French and Spanish Pyrenees and 32 in the Swiss Alps (Fig. 4). Most of the samples were stored in the same container that was used for sampling as shown Fig. 1, so that we could verify the sampling area ourselves. Some samples were provided in a container (e.g. a zipper bag) that was not originally used for sampling. In this case, we relied on the information provided by the person who collected the sample to determine the sampling area (e.g. the diameter of the jar). Among these 152 samples, ~~136~~ 138 were taken within days after the first event in February, and ~~16~~ 14 (2 in the French Alps and ~~14~~ 12 in the Swiss Alps) were collected in March, thus combining the effect of two dust events. The 152 samples were collected by more than 85 individual participants. In the remainder of the text, the analysis was restricted to the ~~136~~ 138 samples that contained only dust from the first event. Table 1 indicates the number of samples used for each type of analysis. Among the 136 samples, only 113 could be analysed due to problems on the remaining 25 (labelling problems, mass outliers, leaks and information missing). For these 113 samples, 20 participants collected one sample, 24 participants two samples, and the rest of the participants collected 3 to 6 samples.
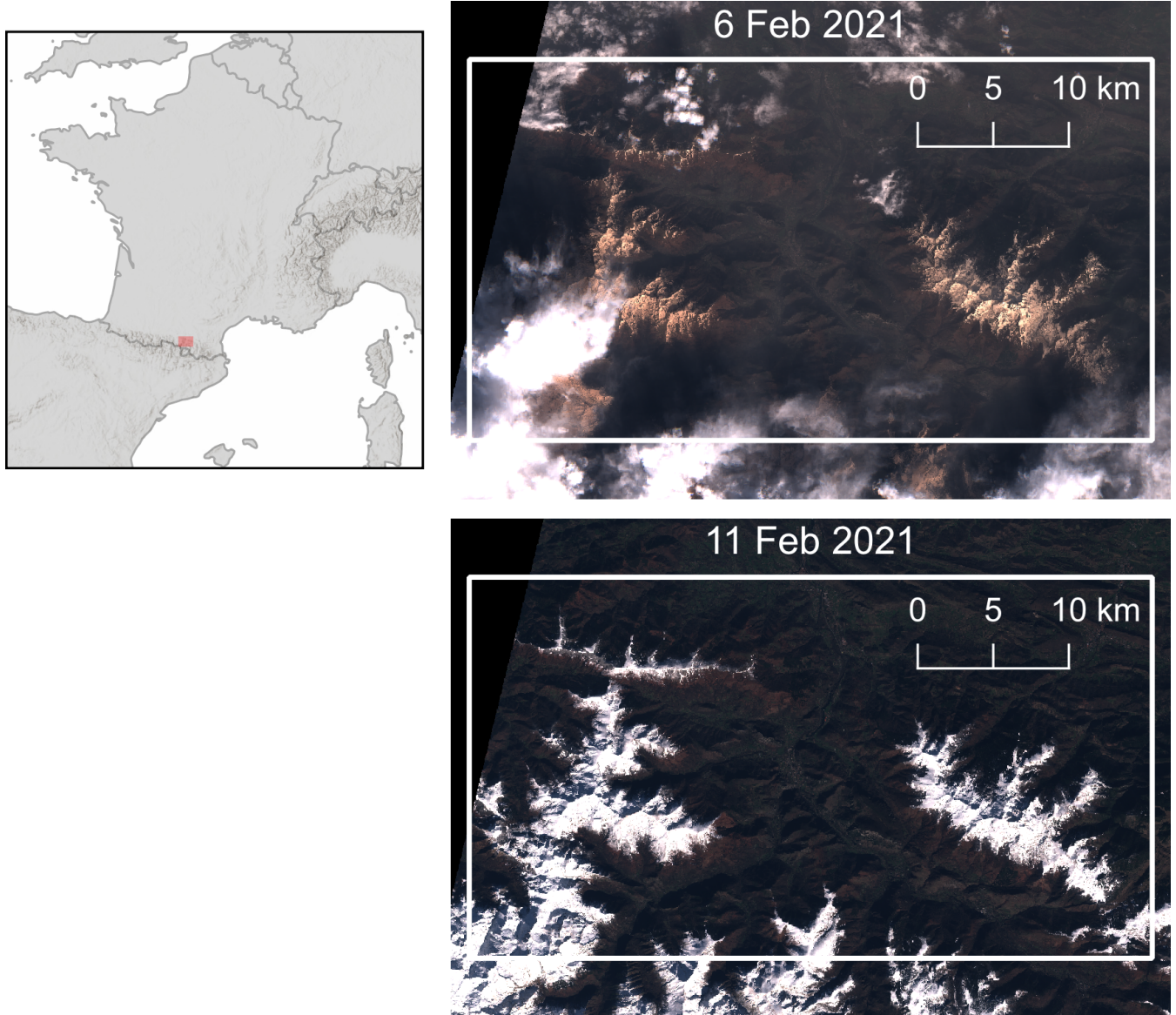
Figure 3. True colour composites of Sentinel-2 images captured on 6 and 11 February 2021. Both images were used to estimate the dust content on 6 February 2021 (the day after the dust deposition).
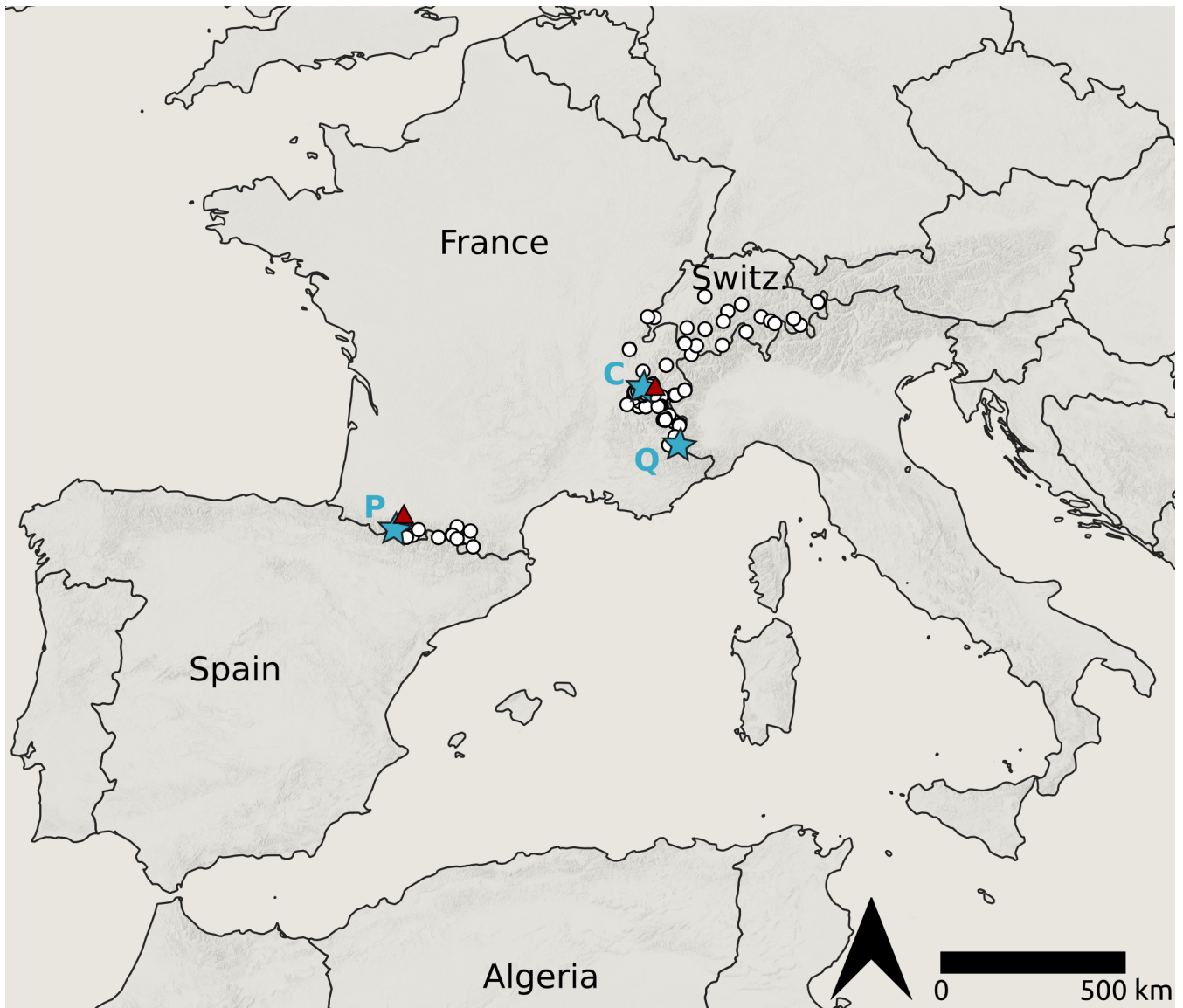
Figure 4. Location of the sample collected during the citizen field campaign. Blue stars indicate the Chartreuse (C), Queyras (Q) and Pic du Midi (P) locations. The red triangle indicates the location of the two samples used for radionuclide analysis

.

3.2 Meteorological conditions

MOCAGE simulations show the hourly meteorological conditions and deposition rates during the dust outbreak that occurred between 4 and 8 February 2021 (see Fig. 5 for Pic du Midi and other sites in supplemental Figs. S2 and S3). At the three selected sites, the snow cover was first affected by dry dust deposition, influenced by southerly winds. Then, during wet deposition, the wind changed to the south-west and west with a decreasing wind speed. According to the simulations for the Pyrenees and the southern Alps, most of the deposition was dry, with 85 and 90% of the total loads at the end of the dry deposition for the Pic du Midi and the Queyras, respectively (Fig. 5, S2). In the northern Alps, the partitioning between wet and dry deposition was approximately half; for instance, 53% of the total load was due to dry deposition at the Col de Porte (Fig. S3). However, some avalanche forecasters in the Pyrenees observed that after 2-3 days of dust in suspension, dust was massively deposited as wet deposition (rain), followed by a graupel shower and then a short snowstorm the following night. Snowfall in the following days covered the dust layer in most parts of the Alps and Pyrenees. However, the dust layer remained easily identifiable in the snowpack below the clean snow layers by digging a snow pit.

3.3 Dust mass and size distribution

3.3.1 Dust mass

A total of ~~114~~ 113 sample-derived masses were obtained over the Alps and the Pyrenees. The missing values (approximately 16%) were due to leaks, which made the samples unusable. These 113 samples correspond to 70 different locations and were mostly sampled by citizens except for the swiss samples (Tab. 1). We believe that there is no systematic difference between the samples collected by citizens and the samples collected by research labs since the measurement protocol was new to both the public and the professional practitioners.

Fig. 6 displays the spatial distribution of the dust mass per unit area obtained from in situ measurements. The dust mass per unit area ranges from 0.2 to 58.6 g m^{-2} depending on the location, highlighting strong spatial variability. The mean value is 9.4 g m^{-2} when considering all the samples. Higher dust depositions are observed in the Pyrenees (Fig. 7A), with a mean mass per unit area of 21.2 g m^{-2}, compared to the French Alps (7.2 g m^{-2}) and the Swiss Alps (4.5 g m^{-2}). This suggests a decrease in the deposited mass along the plume trajectory with distance from the source in the Sahara (Fig. 7B).

These measurements allow us to estimate that the MOCAGE simulation underestimates the deposition fluxes. The modeled deposition fluxes are 0.31, 0.11 and 0. 52 g m^{-2}, while the mass measured from the three closest samples are 14.2, 5.6 and 2.1 g m^{-2}, for the Pic du Midi site, Queyras site and Chartreuse site respectively. This means that MOCAGE simulation underestimates the deposition fluxes by a factor equal to 51.6 for the Pic du Midi site, 13.5 for the Queyras site and 36.4 for the Chartreuse site (Sect. 3.2).

The distribution of dust mass per unit area with slope aspect indicates that a larger dust mass per unit area is generally observed for the south and south-west facing slopes in all three studied areas (Fig. 7C). This conclusion holds both when slopes are computed from a 25 m resolution digital elevation model (Fig. 7C) and from a 500 m resolution DEM (Fig. 7D).
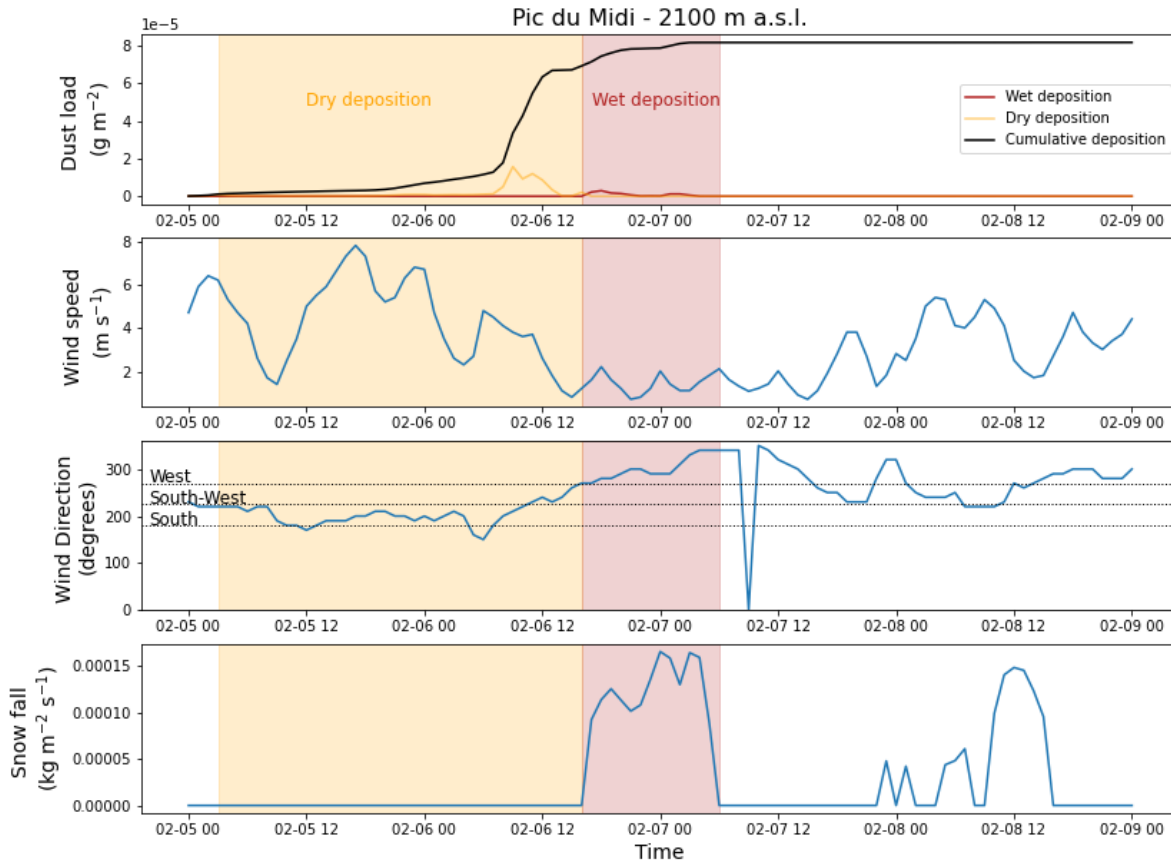
Figure 5. (A) Temporal evolution of the hourly dry (yellow) and wet (red) dust loads during the event at Pic du Midi (2100 m a.s.l.). The total cumulative mass deposition is shown by the black line. Depositions were computed based on MOCAGE outputs and corrected according to the observations (i.e. the measured mass of the three closest samples of the site, see Sect. 3.3.1). The dry vs. wet deposition was determined based on SAFRAN precipitation data (see section 2.2). Temporal evolution of the hourly wind speed (B) and direction (C) and the hourly precipitation (D) from SAFRAN reanalysis data. The yellow (red) shaded area represents the dry (wet) deposition of the event, according to SAFRAN precipitation.

This indicates that dust deposition prevailed on slopes facing the dominant wind during the event (see video supplement, Fig. 5, S2 and S3).

The dust mass per unit area does not show a gradient with elevation (not shown). This result could be due to the sampling pattern, covering a restricted elevation range: 45% of the samples were collected between 1500 and 2000 m a.s.l. and 26% between 2000 and 2500 m a.s.l. Only three samples were collected below 1000 m a.s.l. and one above 2500 m a.s.l.

3.3.2 Dust size distribution

Most of the samples analysed for mass could be analysed for size distribution (Tab. 1). A total of 95 samples were analysed with the Coulter counter, providing 95 size distribution values over the Alps and Pyrenees (Fig. S4). The missing samples result from labels mishandling, ambiguous labeling or other lab mishaps. The distribution tails show the ~~occurrence of a fraction of rather large particles with diameters around 50~~regular occurrence of particles larger than the cutoff diameter ($35-70$ μm , Fig. S4, central right panel), whereas the mean diameter of the well-measured fraction of the distribution is much lower, around 19 μm for the volume distribution and 12 μm for the surface distribution. ~~This analysis shows that adding~~ The cutoff diameter varies with the mean volumic diameter (Fig. S4, right panel) : detecting enough big particles to have a good counting statistics implies a larger mean volumic diameter and a higher cutoff diameter. The cutoff diameter should therefore be seen as an estimate of a potential measurement bias. Adding the distribution tail into ~~calculating~~ the calculation of the average diameters slightly influences the average volume diameter.

The volume distribution can be converted into a mass estimation using a dust density of 2.5 g cm^{-3}, which can be compared to the gravimetric measurement on the filters (Fig. S4, left panel). This comparison shows that the distribution tail, poorly measured with the Coulter counter, actually represents most of the dust mass. This underestimation is likely related to large particles (diameter larger than 50 μm) as shown on the second panel in Fig. S5).

The mean dust diameter measured with the Coulter counter spans a range of 8 to 38 μm when considering the samples over all the massifs. The maximum size may be underestimated due to the size cut-off (see section ~~3.3.2~~2.3). The dust size distribution depends on the location, with larger sizes generally observed closer to the source (Fig. 8B). In the Pyrenees samples, the size spans a range of 15.4-27 μm (with a ~~mean~~ volume average diameter of 21 μm) and varies between 9.8 and 38 μm (~~mean~~ volume average diameter = 21 μm) and 8.2 and 19.6 μm (~~mean~~ volume average diameter = 15 μm) for the French and Swiss Alps, respectively~~(Fig. 8A)~~. Figure 8A shows the same gradient for the surface average diameter. Contrary to the mass distribution, there is no evidence that the dust size is related to the slope aspect (Fig. 8C, D), and we did not find a trend with elevation in the dust mass distribution either.

3.4 Elemental composition

~~105 samples were analyzed for~~ From the 113 samples analyzed for mass, 70 were analysed for the elemental composition since only the filters with a smooth surface could be used for this analysis (Tab. 1). No major contamination with trace metals could be detected in the filters. The concentration of contaminants such as Pb remains low for most of the filters, i.e., close to the natural value for the upper continental crust (17 μg kg^{-1}). However, one sample (Alp-60) has a large concentration (>100
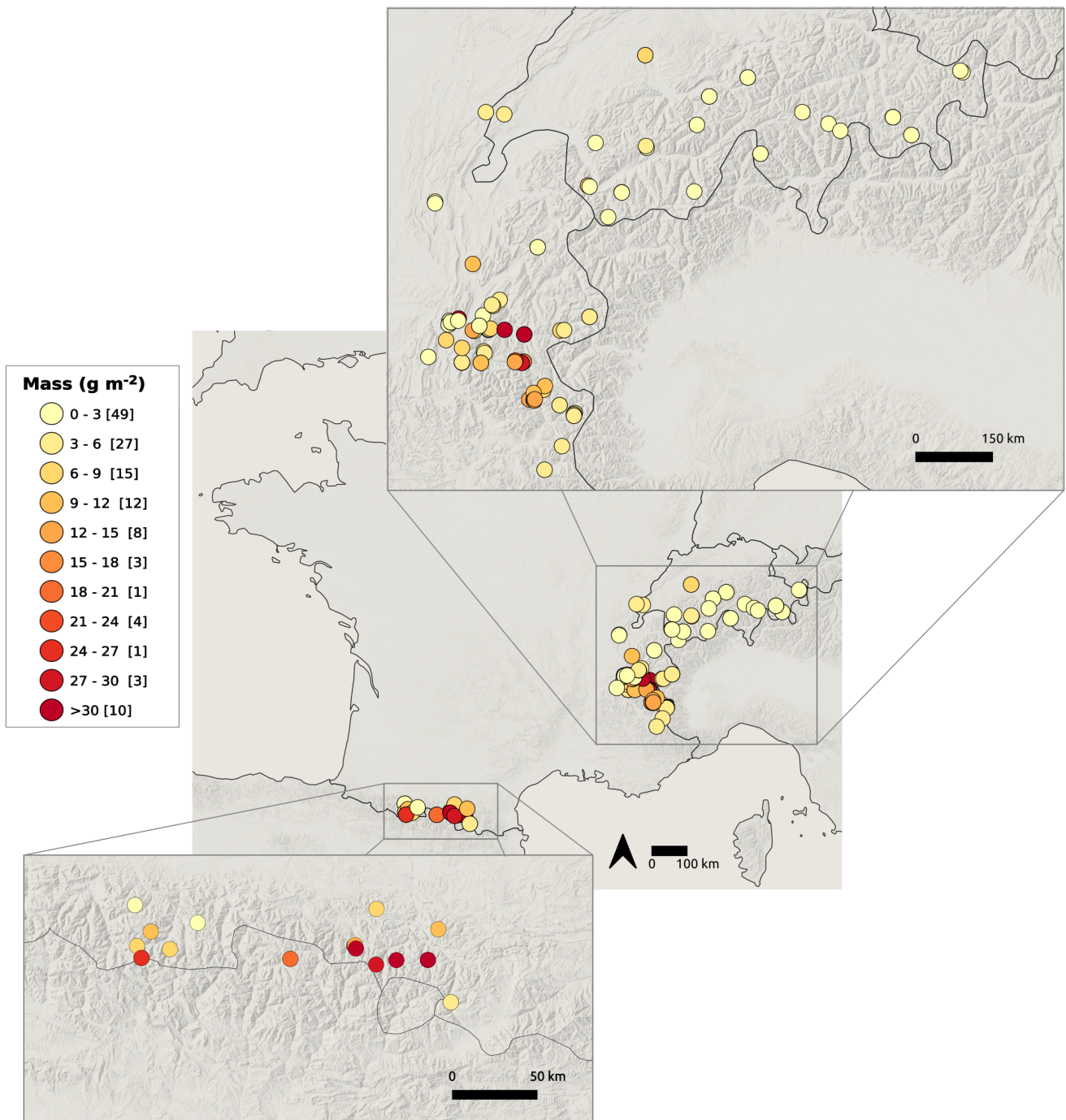
Figure 6. Mass of deposited dust per unit area. The number in brackets in the legend indicates the number of samples.

Mass (g m^{-2})

- 0 - 3 [49]
- 3 - 6 [27]
- 6 - 9 [15]
- 9 - 12 [12]
- 12 - 15 [8]
- 15 - 18 [3]
- 18 - 21 [1]
- 21 - 24 [4]
- 24 - 27 [1]
- 27 - 30 [3]
- >30 [10]
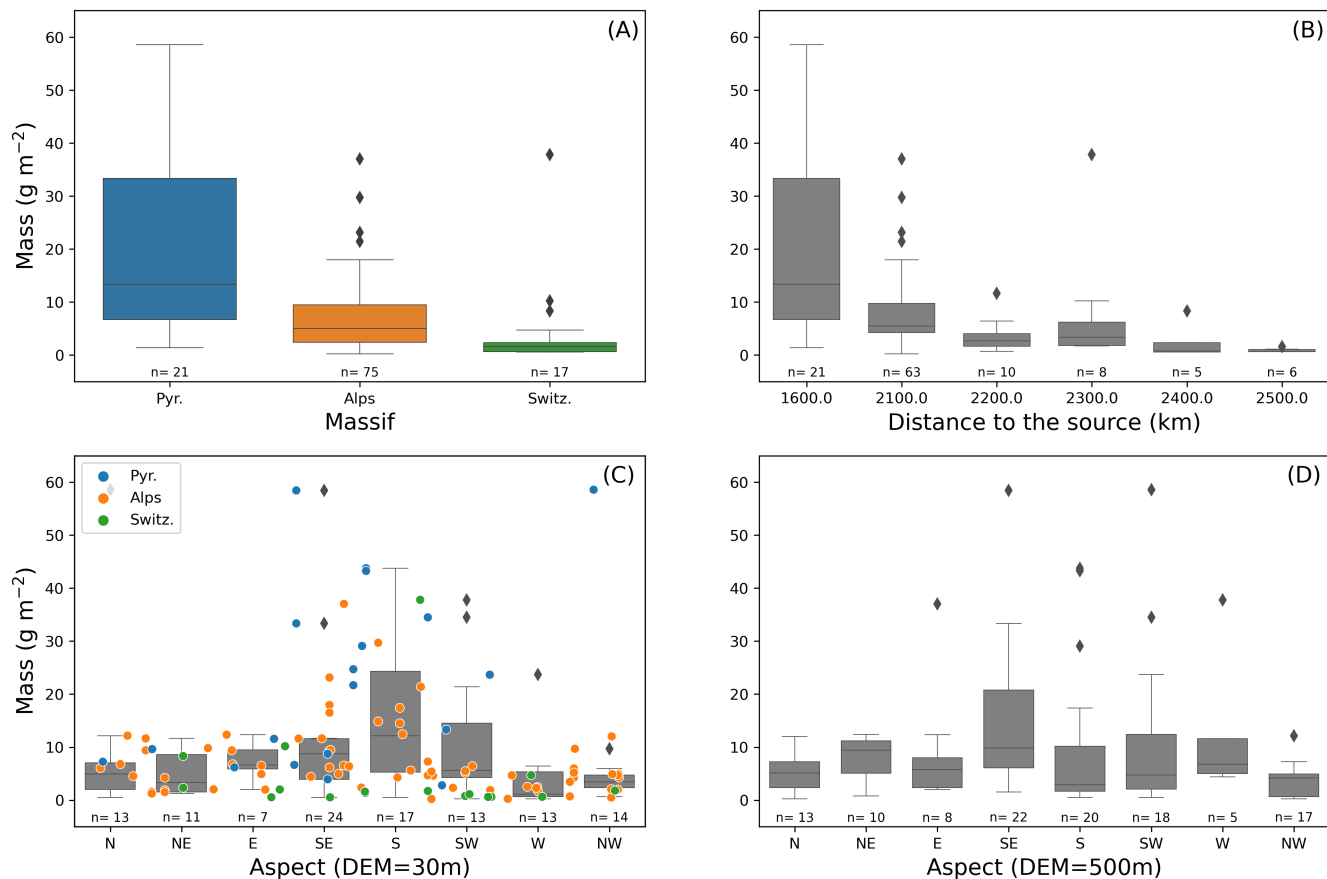
Figure 7. Distribution of the deposited mass dust per unit area against the massif (A), the distance to the source (B) and the aspect computed with a 25 m resolution DEM (C) and a 500 m resolution DEM (D). The boxes show the quartiles of the distribution corresponding to the spatial variability. Minimum/maximum ranges are indicated by the whiskers, and outliers are represented by the black points. The distance to source is estimated from the location 31.21N, -0.37E, estimated from MOCAGE data (video supplement).

$\mu g\, kg^{-1}$). Clear spatial trends can be identified for elemental concentrations depending on the mountain range. Concentrations

265 of Ca, Fe, Mn and Ti decrease from the Pyrenees to the Swiss Alps, while an opposite trend is identified for Al, P and Si, and no trend is observed for K (Figs. 9 and 10), showing concentration dispersion for each mountain range and against distance to the source). Since the mass deposition is much higher in the Pyrenees (Fig. 7A), the elemental deposition density is higher for all elements in the Pyrenees (Fig. 12).

We also investigated the spatial variability of the ratio between elemental concentrations. Figure 11 shows the variability of

270 the Si/Al and Fe/Ca ratios and that of the mass fraction of Fe. The values for Si/Al vary between 1.7 and 2.8. The ratio between Fe and Ca varies between 1 and 2. The values for the Swiss samples are likely unreliable given their very low Ca concentrations (Fig. 12). The mass fraction of Fe varies from 2% to almost 11% from the Swiss mountains to the Pyrenees.
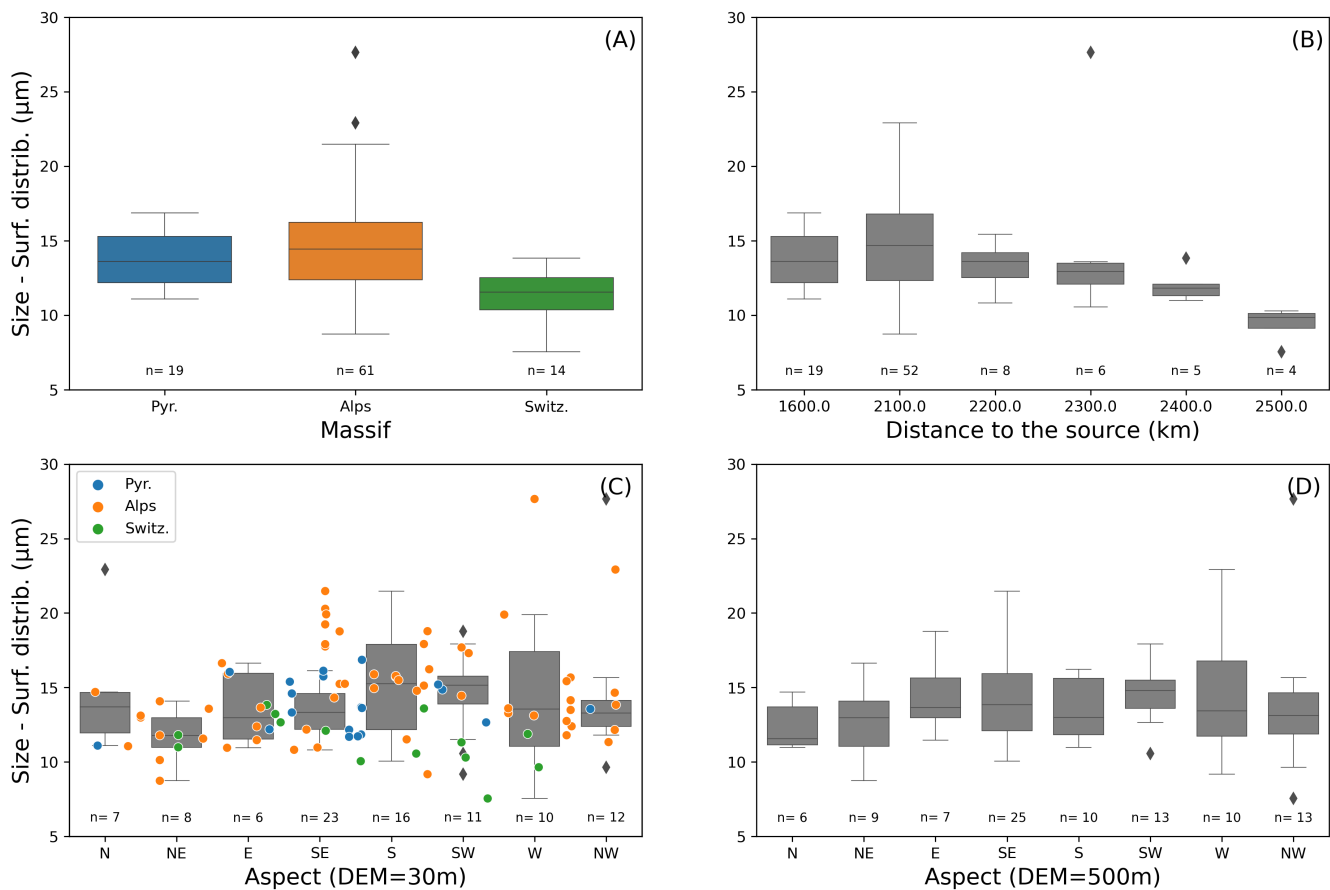
Figure 8. Distribution of the surface average diameter (proxy of the particle size) of the dust deposition against the massif (A), the distance to the source (B) and the aspect computed with a 30 m resolution DEM (C) and a 500 m resolution DEM (D). The boxes show the quartiles of the distribution corresponding to the spatial variability. The number of values used is indicated under each box. Minimum/maximum ranges are indicated by the whiskers, and outliers are represented by the black points. The size for each massif, against the aspect, is shown in Figure (C).

Using a digital microscope, we found plastic fibres in a few samples. This means that local contamination may affect the results of some analyses. However, it has likely not influenced the elemental concentrations of the filters.

3.5 Optical properties

The infrared normalised extinction spectra obtained for the two samples are very similar (Fig. 13). The main feature at 1035 cm^{-1} can be assigned to the asymmetric stretching of the Si-O-Si bond of illite. From 1500 cm^{-1}, the extinction gradually increases due to scattering with a steeper slope for the Pic du Midi sample compared to that of the Lautaret. This can be explained by the higher values of $\overline{d_g}$ and σ_g for the Pic du Midi sample. These spectra have been smoothed by applying the Savitzky-Golay filter to identify other bands. A zoom (650–2000 cm^{-1}) for each spectrum is shown in Figure S6 with the assignment of all the characteristic bands of illite, quartz and calcite (see also Table 2).

Using Equation 3 below, we simulate the extinction spectrum for the two samples by calculating a linear combination of the extinction spectra of the three minerals identified in Figure S6:

$$\Gamma_{sample}^{simul} = \sum_i C_i \Gamma_i \tag{3}$$

where Γ_i is the extinction spectrum of the mineral i and C_i are coefficients that are fitted by a least-squares fitting method minimising the differences between the calculated extinction and the experimental extinction ($i = q$, il and c for quartz, illite and calcite). The calculation of the extinction spectrum for each mineral was performed using Mie optical theory (Herbin et al., 2017) by introducing their complex refractive indices (CRI) recently determined by Deschutter (2022) as input data and a size distribution calculated using the fitted moments of the distribution listed in part 6.3.1. of Deschutter (2022).

The simulated spectra, as well as the differences, $\Gamma_{sample}^{simul} - \Gamma_{sample}$ are plotted in Fig. S6 for the two samples. The simulated extinction spectra fit very well with the experimental spectra, especially in the spectral window of 750–1550 cm^{-1} where the mean relative difference is less than 5%. There are no direct relationships between the coefficients listed in the legend of Fig. S6 and the concentrations of the minerals in the two natural samples, but it gives trends for the relative proportion of each mineral. Both samples likely contain a large proportion of illite compared to quartz and calcite. The Pic du Midi sample does not contain calcite because $C_c = 0$ for this sample.

To estimate the mass extinction efficiency (MEE), the mass concentration is derived from the fitted size distribution assuming spherical particles with a mean density of $\rho_p = 2.7$ g cm^{-3}. The values of the MEE are reported in Fig. S7 in the 650–4000 cm^{-1} spectral range. The maximum MEE is 0.39 m^2 g^{-1} at 1035 cm^{-1} and 0.25 m^2 g^{-1} at 1035 cm^{-1} for the Lautaret and Pic du Midi samples, respectively.

3.6 Radionuclide analyses

The combination of both the low quantity of dust material collected on the filters (= 0.3 g) and their relatively low activity in artificial radionuclides was insufficient to quantify the content in ^{137}Cs (< 11.9 Bq kg^{-1}) in the dust filter with the highest dust quantity (0.3 g). In a sample with a similar material quantity and prepared under the same conditions but containing higher
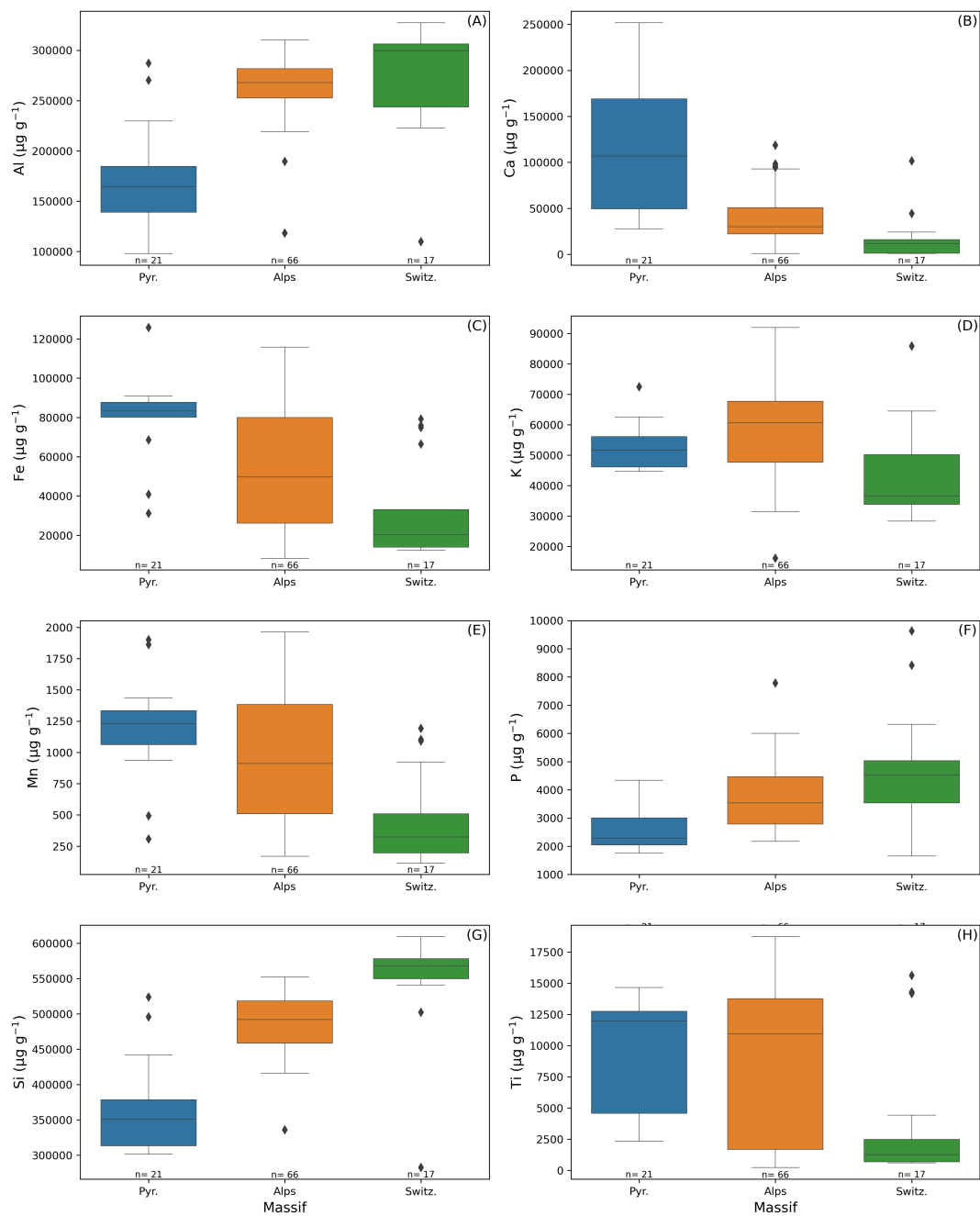
Figure 9. Distribution of elemental concentrations against the massif (A) Aluminium, (B) Calcium, (C) Iron, (D) Potassium, (E) Manganese, (F) Phosphorus, (G) Silicon and (H) Titanium. The boxes show the quartiles of the distribution corresponding to the spatial variability. The number of values used is indicated under each box. Minimum/maximum ranges are indicated by the whiskers, and outliers are represented by the black points.

^{137}Cs activities (IAEA-444 soil material), this ^{137}Cs activity could be quantified (72.9 ± 8.5 Bq kg^{-1}) in good agreement with the certified value (68.5 ± 1.4 Bq kg^{-1}).

With a higher quantity of dust material available (i.e., 13 g), the Barèges sample showed a ^{137}Cs activity of 19.0 ± 0.5 Bq kg^{-1}. This activity is higher than that typically observed in the upper layer of soils collected ca. 40° north (5 ± 2 Bq kg^{-1}), which is likely explained by the very small particle size of dust deposited, as clays are known to be enriched in fallout radionuclides (Evrard et al., 2020).

In addition to ^{137}Cs detection, the activities in natural fallout radionuclides that were well detectable in both the ALP-34-FE filter and the much more abundant dust sample from Barèges demonstrated that both dust samples collected in 2021 were strongly tagged by short-lived radionuclides associated with rainfall (^{7}Be/^{210}Pb$_{xs}$ ratios > 4), demonstrating their very recent deposition or their recent exposure to precipitation. These ratios are consistent with those analysed in other wet rainfall samples across Europe, as reviewed by Gourdin et al. (2014), and they remained of the same order of magnitude as those (> 4) analysed in fresh sediment collected in Central France by Le Gall et al. (2017).

We found that the ^{240}Pu/^{239}Pu isotopic signature of the Barèges dust sample was 0.173 ± 0.008.

3.7   Satellite data

Figure 14 shows the large spatial variability of the satellite-derived dust content, ranging from 0 to 8000 ppm. The dust concentration obtained from the satellite is retrieved as a mass fraction (mass of dust per unit of snow mass, see Sect. 2.7) and hence is not directly comparable to the dust mass obtained from the in situ samples (in kg m^{-2}, i.e., a mass per unit area). However, we observe a similar distribution of both quantities with the terrain aspect, with increased dust amount on south facing slopes in both datasets (Fig. 7).

4   Discussion

The analysis of the samples reveals the strong spatial variability of the deposition rates, with higher mass found at the locations where the dust plume arrived first (Pyrenees, mean 21.2 g m^{-2}) than at the locations where the dust was deposited the latest (Swiss mountain ranges, mean 4.5 g m^{-2}). A similar spatial trend is found in the particle size with a decrease in mean diameter from 21 (Pyrenees) to 15 μm (Switzerland). For the mass only, this large-scale pattern is superimposed on a more local gradient, as we find more dust mass on the south and south-east facing slopes at the massif scale. This gradient is evident from the snow samples but also from remote sensing data. This suggests that large-scale monitoring using satellite data should be possible, although further work is needed to establish a more direct comparison and therefore evaluate the uncertainty of such retrievals. Because the wind was blowing from the south and south-east during the dry deposition event, the higher accumulation on south facing slopes is consistent with the orographic effect (Mott et al., 2018). Regarding the dust size distribution, the comparison between the mass measured on the filters and the mass estimated from the size distribution shows that a substantial part of the dust mass is likely related to large particles, with a diameter larger than 50 μm (mass fraction likely higher than 50 %). Other

335   studies have reported long-range transport of giant dust particles (with a diameter larger than 100 μm) (Varga et al., 2021; Adebiyi et al., 2023).

     The elemental composition of the samples also exhibits a large-scale gradient except for potassium. Fe/Ca and Si/Al ratios are similar to other values found in the literature for Saharan dust (Caponi et al., 2017), while the mass fraction of iron decreases from 11 % in the Pyrenees to 2 % in the Swiss mountain ranges. This wide range of values was also reported in Di Biagio et al.

340   (2019). In the latter study, it is also shown that the optical properties of the dust strongly vary with the elemental iron, suggesting that the optical properties of the dust in the UV-VIS-VNIR range vary along transport within this single dust deposition event.

     For the radionuclide analyses, the results obtained on the 13-g Barèges sample show that this larger sample quantity greatly facilitates gamma spectrometry measurements and collecting a sample quantity of at least $\approx$10 g of dust could therefore be an objective in the case of future occurrence of Saharan dust episodes in Europe, should other participatory dust collection cam-

345   paigns be initiated. In addition to ^{137}Cs detection, obtaining such a larger quantity of material would allow a better multiproxy characterisation of the dust, not only in gamma-emitting radionuclides (e.g., ^{137}Cs, ^{7}Be and ^{210}Pb) that can be quantified using physical and nondestructive measurement techniques but also in alpha-emitting radionuclides (e.g., Pu isotopes), which require time-consuming and destructive analyses (the typical test catch is 5 g per sample for Pu analyses).

     The plutonium analyses conducted on the Barèges dust sample showed that the ^{240}Pu/^{239}Pu isotopic signature of this sample

350   (0.173 $\pm$ 0.008) perfectly matches that of the global fallout in the Northern Hemisphere (0.176 $\pm$ 0.007) largely dominated by USA and USSR thermonuclear tests conducted in the late 1950s and the early 1960s (Kelley et al., 1999). This is also corroborated by the $^{239+240}$Pu/^{137}Cs value of 0.021 found for the Barèges sample, remaining in the global fallout range (0.018-0.030) (UNSCEAR, 2008). These results confirm those obtained on Saharan dust samples collected in Southern France in 2004 (Masson et al., 2010). Although the ^{240}Pu/^{239}Pu isotopic signature of the fallout associated with the few atmospheric

355   French nuclear tests conducted in the Sahara has not yet been published in public, it is unlikely that this signature perfectly coincides with that of the so-called global fallout (given that different types of bomb engines and fuels were used by the different countries). Accordingly, the public assertion that the ^{137}Cs borne by Saharan dust originates from the French nuclear tests conducted in the Sahara between 1960 and 1966 is likely wrong (Berger, 2021). It is more likely to correspond to ^{137}Cs released by the much more numerous and powerful tests conducted by the USA and the USSR in the Northern Hemisphere

360   between 1954 and 1963 (French tests corresponded to 0.017% of the total power generated by the worldwide tests during this period according to data from UNSCEAR (2008)). Nevertheless, more work is needed to define the Pu isotopic signature of the French test fallout in the Sahara. Furthermore, more dust samples collected at different locations should be analysed to confirm the current results.

     Saharan dust plays an important role in the biogeochemical cycles of nutrient-poor environments such as some oceanic

365   areas, tropical forests and high-altitude oligotrophic lakes. A Saharan deposition event could supply an important proportion of the minerals, especially phosphorus inputs in high-altitude areas (Okin et al., 2004). Gross et al. (2015) examined phosphorus concentrations for five dust events over Cape Verde. P concentrations were highly variable, ranging from 1500 μg g^{-1} to 5500 μg g^{-1}. Our dataset shows that for a single event, the concentration range increased with distance from the source: while P concentrations were homogeneous in the Pyrenees (959+/-215 μg g^{-1}), a larger dispersion was observed in the Swiss Alps

370 (1738+/-637 μg g^{-1}). Dam et al. (2021) showed that P speciation evolves while crossing the Atlantic Ocean. The larger the distance from the source along the transport path, the more Fe/Al-P and less Ca-P minerals are present in the dust in relation to particle sorting and weathering. The homogeneous sampling of a single event that we performed in the current research showed similar behaviour, with a relative enrichment in P and Al and a relative loss of Ca and Fe during transport.

5   Conclusions

375 We presented data from ~~136~~ 113 dust samples collected in snow after a major dust event in February 2021 in south-west Europe. The samples were spatially distributed from the Pyrenees to the French and Swiss Alps, covering a wide range of topographic features. We obtained the samples from a citizen science campaign, which required a simple sampling protocol. We analysed various physicochemical properties, including deposited mass per unit area, particle size, elemental composition, radionuclide concentrations, and optical extinction. To our knowledge, this is the first time that such a large number of dust samples from a

380 single dust event in the Pyrenees and the European Alps were collected and analysed with multiple analytical tools. A second citizen campaign was launched for the second of the two dust events late February 2021 in Finland (Meinander et al.). We provide the results of ~~these~~ our analyses along with the geographic coordinates of every sampling site.

The dataset should be useful to evaluate the skills of atmospheric transport models (e.g. Baladima et al., 2022). The measured properties of the dust could also be used for impact studies, such as for quantifying the impact of the dust on snow cover duration

385 in Europe (e.g. Réveillet et al., 2022).

The analysis of the dataset already revealed noteworthy results:

- We find a gradient in the dust mass and the dust size distribution with the distance along the dust plume. Larger masses and sizes are found at the locations where the dust plume arrived first (the Pyrenees in this case). This gradient is also found in the elemental composition. For instance, the total elemental iron mass is higher in samples from the Pyrenees

390 than in those from the Swiss mountain ranges. This suggests that dust optical properties could vary along transport within a single event. An opposite trend is observed for P, with important implications for the biogeochemical functioning of ecosystems.

- In addition to this large-scale spatial pattern, we find a higher dust mass on the south and south-east facing slopes, suggesting preferential dust deposition on windward slopes.

395 - A plutonium analyses show that the isotopic signature of the dust perfectly matches that of the global fallout in the Northern Hemisphere, contrary to what was announced by the media (i.e., origin associated with the French nuclear tests in the 1970s in the Sahara).

- Sentinel-2 multispectral remote sensing imagery is promising for characterising this spatial variability, although further work is needed to evaluate the uncertainties of this method.

400 It is remarkable to find consistent spatial trends, which are compatible with physical processes despite the heterogeneity of the sample sources of this campaign. Although some participants are snow measurement experts, many others were not trained

to collect environmental samples and data. Tools and containers to collect the samples were not standardised. The sampling method was as simple as possible to avoid discouraging nonexpert people. Therefore, we could obtain sufficient samples to compensate for errors and inaccuracies during the data collection process. However, the sampling protocol of future campaigns should be improved for optical property measurements and radionuclide analyses since more dust mass is needed for such measurements than what could be sampled.

The above results show that involving citizens in the data collection process can lead to scientific advances beyond the current knowledge. This campaign was also a unique opportunity to generate informal exchanges between scientists and citizens. From our perspective as scientists, it was particularly stimulating to meet people curious about our work and supporting our research. We will continue to use this dataset to try to answer some of the key questions that we were asked by the participants. In particular, we aim to better characterise the impact of dust deposition on (i) snowmelt runoff, hydrological resources and ski resort management (Dumont et al., 2020; Réveillet et al., 2022), (ii) glacier mass balance, (iii) avalanche hazard (Dick et al., 2022) (iv) and ecosystem productivity.

Analysis	Total analyzed	Regions	Source	Reference	Comments
Dust mass	113	87 locations Pyr., French Alps, Swizterland	Citizens (95) Res. Labs (19)	circles on Fig. 4 Sec. 2.3, Sec. 3.3.1	152 samples collected 138 of the first dust event 27 with problems
Size distribution	95	87 locations Pyr., French Alps, Swizterland	Citizens (79) Res. Labs (16)	circles on Fig. 4 Sec. 2.3, Sec. 3.3.2	taken among the 113 samples for mass
Elemental composition	70	70 locations Pyr., French Alps, Swizterland	Citizens (54) Res. Labs (16)	circles on Fig. 4 Sec. 2.4, Sec. 3.4	taken among the 113 samples for mass
Additional samples					
Radionuclides	3	Pyr., French Alps.	Res. Labs (2) Citizens (1)	Triangles on Fig. 4 Sec. 2.6, 3.6	need higher mass than the common samples
Optical Properties	2	Pyr., French Alps	Res. Labs (2)	Sec. 2.5, Sec. 3.5	need higher mass than the common samples

Table 1. Overview of all the dust samples analyzed in this study

Vibrational mode	Centre of the band cm^{-1}	Mineral
ν(Si-O-Si) symmetric	782, 800	Quartz
δ(CO3) out of plan	76	Calcite
δ(Al-Al-OH)	917	Illite
ν(Si-O-Si) asymmetric	1034	Illite
ν(Si-O-Si) asymmetric	1100, 1163	Quartz
ν(CO3) asymmetric	1460	Calcite

Table 2. Assignment of the vibration modes (ν: stretching mode and δ: bending mode) with the corresponding mineral
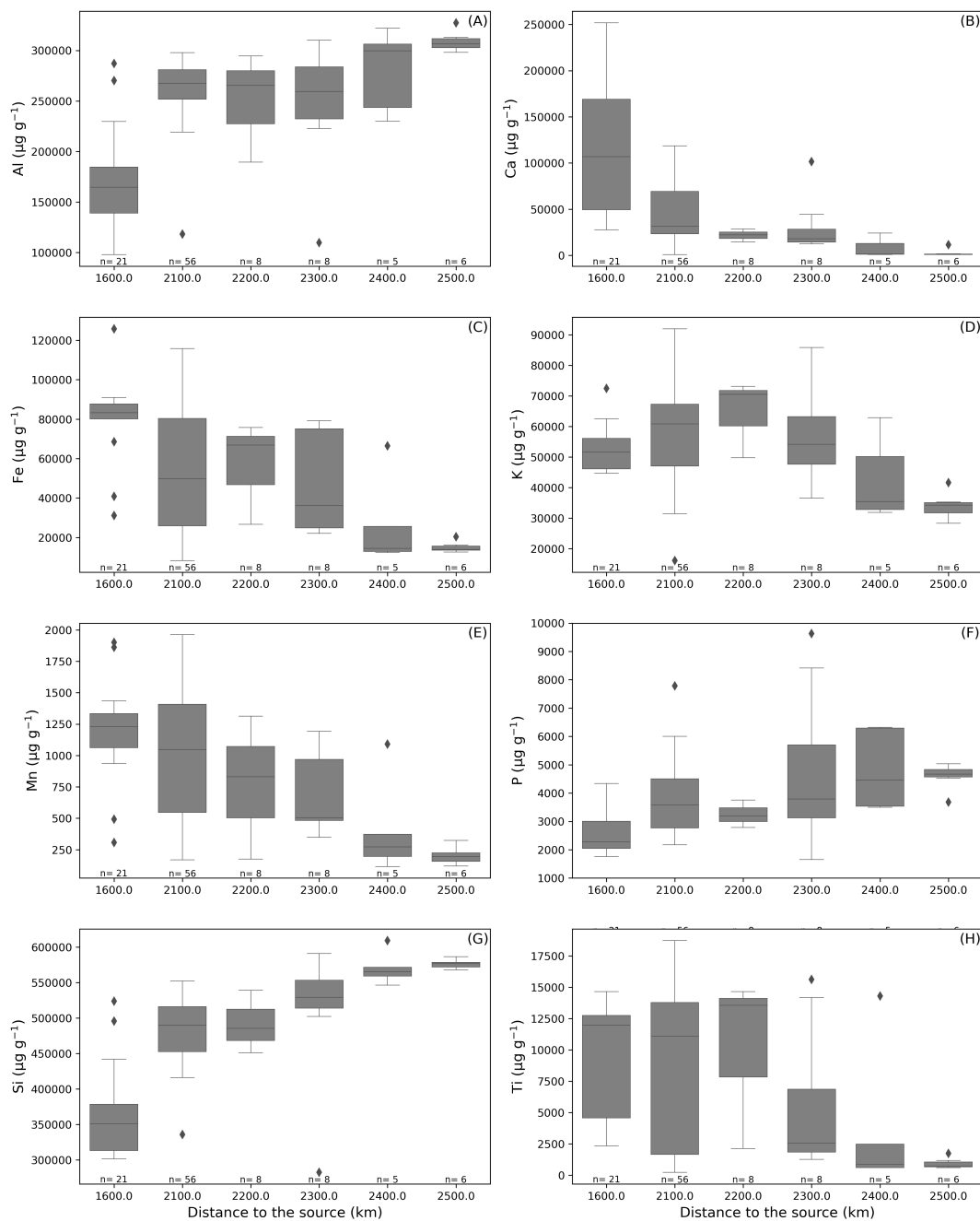
Figure 10. Distribution of elemental concentrations against the distance to the source (A) Aluminium, (B) Calcium, (C) Iron, (D) Potassium, (E) Manganese, (F) Phosphorus, (G) Silicon and (H) Titanium. The boxes show the quartiles of the distribution corresponding to the spatial variability. The number of values used is indicated under each box. Minimum/maximum ranges are indicated by the whiskers, and outliers are represented by the black points.
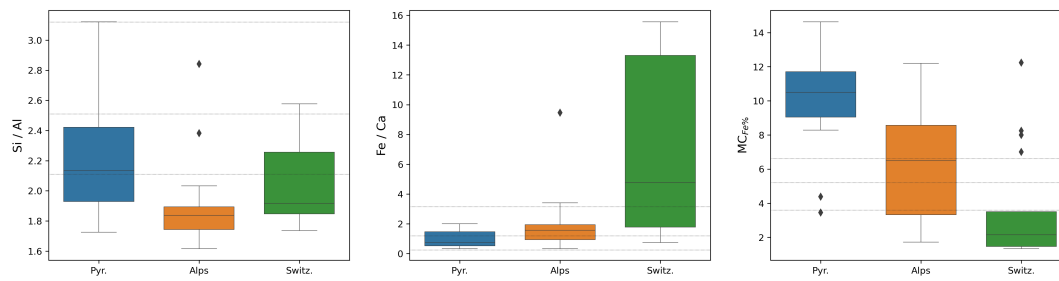
Figure 11. Distribution of elemental ratio against the massif (a) Si/Al, (b) Fe/Ca, and (c) mass fraction of Fe. The boxes show the quartiles of the distribution corresponding to the spatial variability. The number of values used is indicated under each box. Minimum/maximum ranges are indicated by the whiskers, and outliers are represented by the black points. The black horizontal corresponds to the values provided in Table 3 of Caponi et al. (2017) for Saharan dust PM10.6.
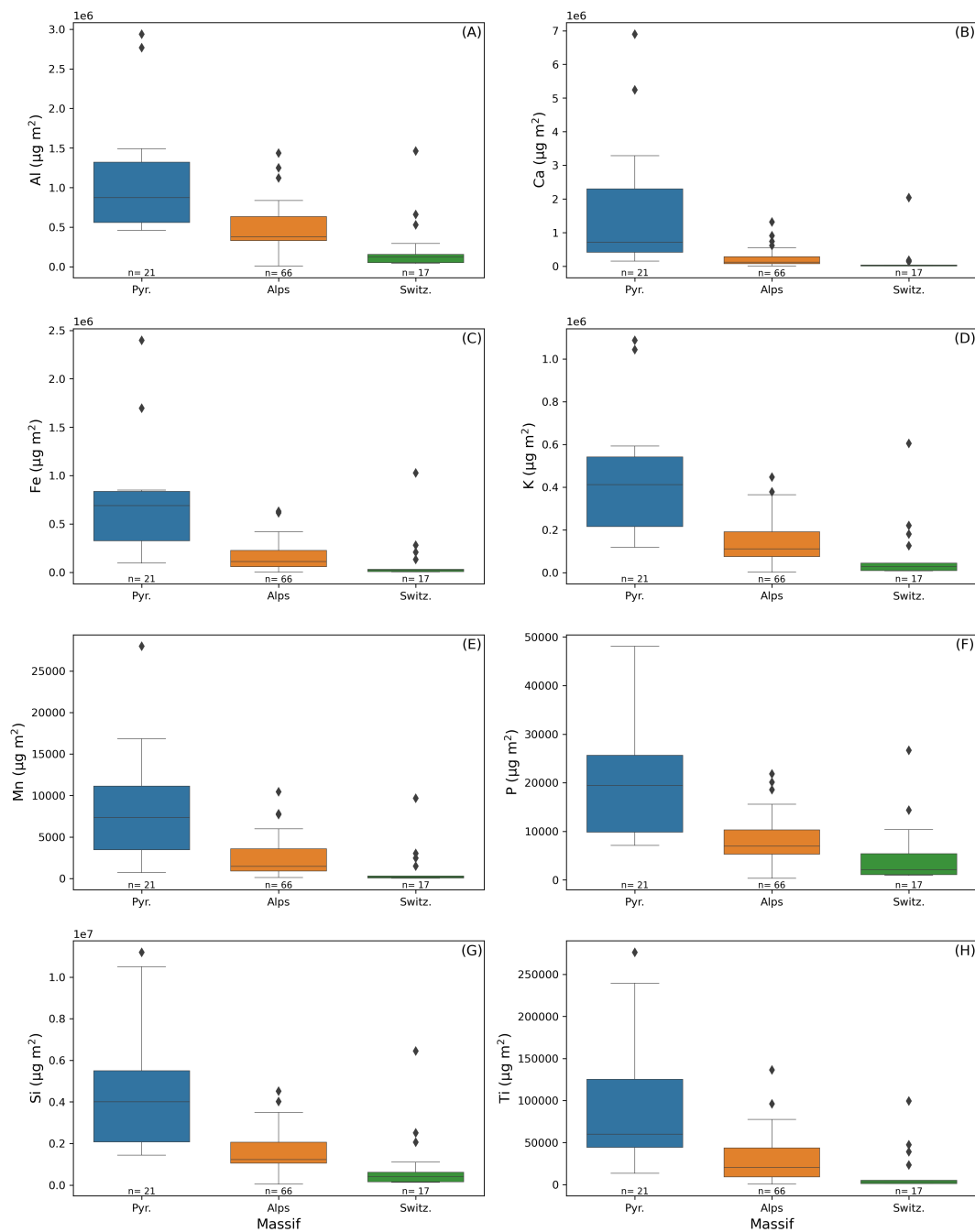
Figure 12. Distribution of elemental mass against the massif (A) Aluminium, (B) Calcium, (C) Iron, (D) Potassium, (E) Manganese, (F) Phosphorus, (G) Silicon and (H) Titanium. The boxes show the quartiles of the distribution corresponding to the spatial variability. The number of values used is indicated under each box. Minimum/maximum ranges are indicated by the whiskers, and outliers are represented by the black points.
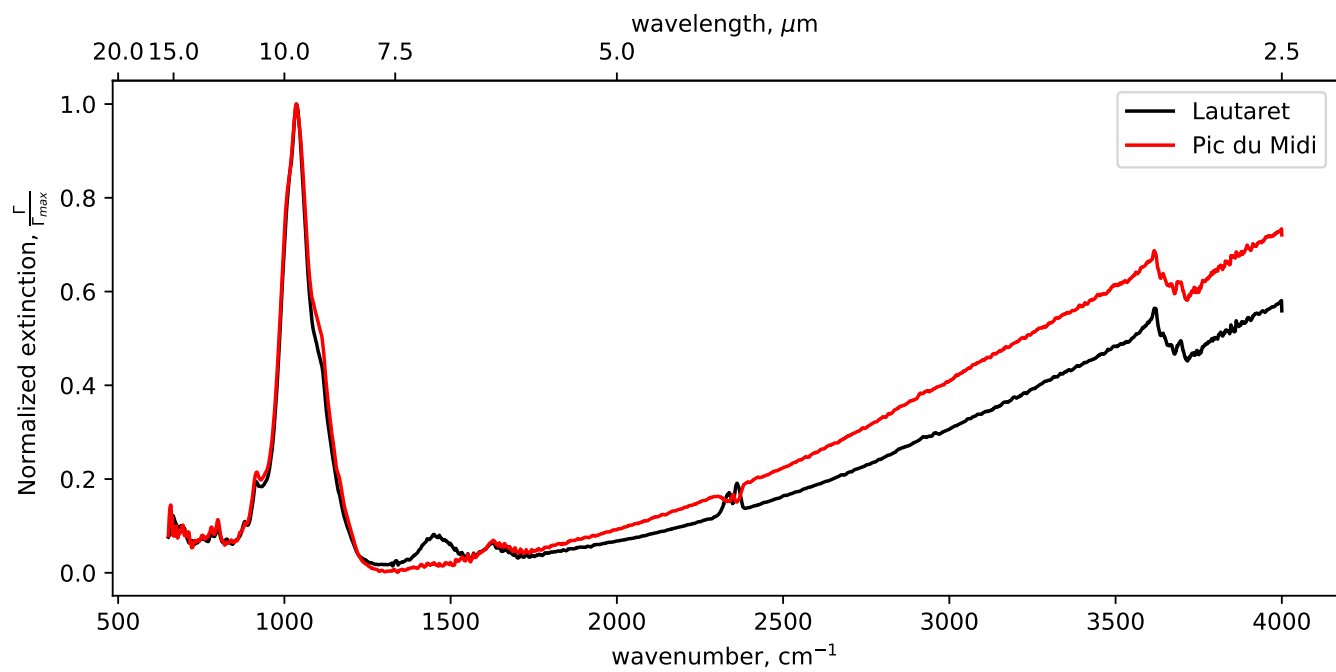
Figure 13. Normalised extinction spectra for dust sampled at Lautaret and Pic du Midi. The bands observed at 2350 cm^{-1} are due to the absorption of residual CO_2 in the cell.
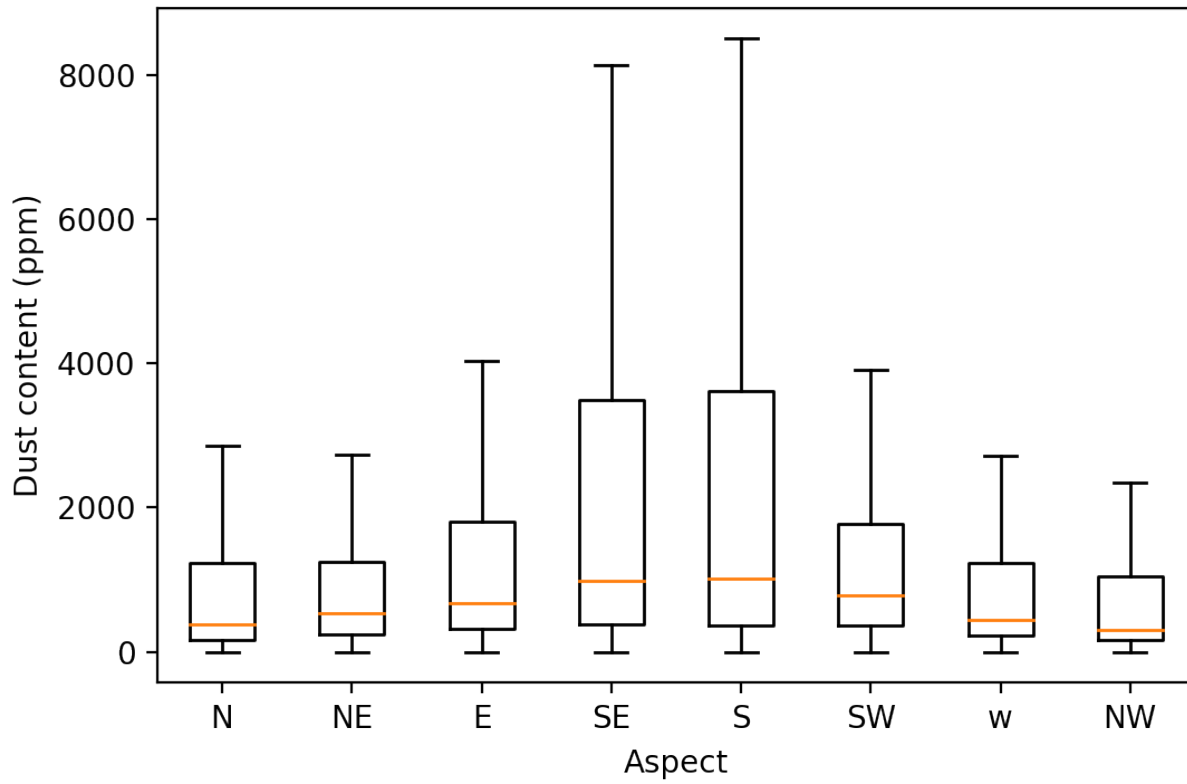
Figure 14. Dust content on 6 February 2021 in the Tabe and Vicdessos massifs (Pyrenees) from Sentinel-2 data aggregated by aspect classes. The box extends from the lower to upper quartile values of the data, with a line at the median. Outliers were not plotted.

Data availability. Data presented in this study are available at https://doi.org/10.5281/zenodo.7969515 (Dumont et al., 2022). The dataset contains the mass and size data for each sample, as well as the exact coordinates of each sample. It also contains the elemental composition of the samples, as well as the calibration function of XRF. A data file is also provided for the optical properties (MEE and extinction) and for the radionuclides analysis.

Video supplement. The video is available at: https://doi.org/10.5281/zenodo.7457613

Author contributions. M.D., S.G., D.V. and S.M. designed the citizen campaign. A.F. collected a dust sample in Barèges. O.E., I.L. and A.D. conducted the radionucleide analyses. G.L.R., L.G. and S.H. conducted elemental composition analysis. F.T. and M.R. participated to the data analysis. A.G. and C. V. performed the mass and coulter measurements. A. D., D. P., H. H. performed the optical properties measurements. J. T. and M. S. coordinated the swiss sampling. L. A., M. B., M. B. P., C. C., L. D., F. F., A. F., M. F., I. G., P. H., B. J., Q. L., P. S., L. L., A. R., E. T., M. V., L. V.-G. participated to the sampling. B. J. provided the MOCAGE data. M.D., S.G. and M.R. wrote the paper with contributions from all co-authors.

Competing interests. The authors declare that no competing interests are present.

Acknowledgements. The authors are thankful to G. Picard for help in designing the field campaign, F. Besson and M. Jeoffrion for their support with the MOCAGE data, C. Lefebvre and L. Fouassier for help with the XRF analysis. P-XRF instruments were generously loaned by the GEODE laboratory (M. Philippe) and the ATCAF project (ANR-21-CE34-0001 to S. Hansson). We deeply thank the 87 citizens who collected the samples and made this study possible (J.L. Ottenio, M Fructus, I. Lecot, C. Lauvernet, L. , L. Lombard, M. Lhote, M. Fontanille, R. and J. Gottardi, G. Ballini, F. Estival, F. Mandel, M. Barral, A. Durain, J. Grisillon, M. Raveton, M. Chapuis, J. Puig, , C. Ogier, L. Guy, C. Hubert, F. Gillet, D. Rouanoux, F. Pikorki, M. Fontanil, V. Barthes, B. Gombert, C. Wendel, M. Bacardit, L. Koechlin, E. Mougin, L. Zawadzki, L. Dufour, A. Barnoud, J. Saussede, A. Cluzet, M. Beguin, B. Malan, D. Menez, P. René, L. Voisin, Lilyane H., S. Grenier, O. Antoire, F. Pikorki, R. Pilon, B. Luks, B. Frere, C. Mercier, J. Grisillon, F. Miller, J. B. Portier, V. Clouard, N. Robbe, H. Löwe, Schneiter, S. Jourdan, A. Putey, R. Tessier). We thank the observers at SLF for their spontaneous additional sampling efforts (P. Schneiter, H. Rhyner-Elmer, G. Darms, J.-P. Wagnières, R. Troillet, V. Bettler, P. Schneiter, A. Heim, R. Tomamichel, C. Egler, G. Valenti, P. Erne, B. Bournissen, J.-L. Lugon, G. Kappenberger). This work was funded by ANR grant EBONI (ANR-16-CE01-0006). M. Dumont has received funding from the European Research Council (ERC) under the European Union's Horizon 2020 research and innovation programme (grant agreement no. 949516, IVORI). This work is a contribution to the LabEx CaPPA (Chemical and Physical Properties of the Atmosphere) project funded by the French National Research Agency (ANR) under contract ANR-11-LABX-0005-01 and to the Regional Council Hauts-de-France CPER research project CLIMIBIO. CNRM/CEN and IGE are part of Labex OSUG@2020 (ANR-10-LABX-0056).

References

Adebiyi, A., Kok, J. F., Murray, B. J., Ryder, C. L., Stuut, J.-B. W., Kahn, R. A., Knippertz, P., Formenti, P., Mahowald, N. M., Pérez García-Pando, C., Klose, M., Ansmann, A., Samset, B. H., Ito, A., Balkanski, Y., Di Biagio, C., Romanias, M. N., Huang, Y., and Meng, J.: A review of coarse mineral dust in the Earth system, Aeolian Research, 60, 100 849, https://doi.org/https://doi.org/10.1016/j.aeolia.2022.100849, 2023.

Baladima, F., Thomas, J. L., Voisin, D., Dumont, M., Junquas, C., Kumar, R., Lavaysse, C., Marelle, L., Parrington, M., and Flemming, J.: Modeling an Extreme Dust Deposition Event to the French Alpine Seasonal Snowpack in April 2018: Meteorological Context and Predictions of Dust Deposition, Journal of Geophysical Research: Atmospheres, 127, e2021JD035 745, https://doi.org/https://doi.org/10.1029/2021JD035745, e2021JD035745 2021JD035745, 2022.

Berger, A.: Cesium-137 : les poussières radioactives retrouvées dans le sable du Sahara sont-elles dangereuses ?, section: economie-et-politique, 2021.

Caponi, L., Formenti, P., Massabó, D., Biagio, C. D., Cazaunau, M., Pangui, E., Chevaillier, S., Landrot, G., Andreae, M. O., Kandler, K., et al.: Spectral-and size-resolved mass absorption efficiency of mineral dust aerosols in the shortwave spectrum: a simulation chamber study, Atmospheric Chemistry and Physics, 17, 7175–7191, 2017.

Dam, T. T. N., Angert, A., Krom, M. D., Bigio, L., Hu, Y., Beyer, K. A., Mayol-Bracero, O. L., Santos-Figueroa, G., Pio, C., and Zhu, M.: X-ray Spectroscopic Quantification of Phosphorus Transformation in Saharan Dust during Trans-Atlantic Dust Transport, Environmental Science & Technology, 55, 12 694–12 703, https://doi.org/10.1021/acs.est.1c01573, pMID: 34506717, 2021.

DeCarlo, P. F., Slowik, J. G., Worsnop, D. R., Davidovits, P., and Jimenez, J. L.: Particle Morphology and Density Characterization by Combined Mobility and Aerodynamic Diameter Measurements. Part 1: Theory, Aerosol Science and Technology, 38, 1185–1205, https://doi.org/10.1080/027868290903907, 2004.

Delmonte, B., Petit, J., Andersen, K. K., Basile-Doelsch, I., Maggi, V., and Ya Lipenkov, V.: Dust size evidence for opposite regional atmospheric circulation changes over east Antarctica during the last climatic transition, Climate Dynamics, 23, 427–438, https://doi.org/https://doi.org/10.1007/s00382-004-0450-9, 2004.

Deschutter, L.: Optical properties of Gobi dust and its pure compounds: experimental extinction spectra and complex refractive indices determination, Ph.D. thesis, University of Lille, 2022.

Di Biagio, C., Formenti, P., Balkanski, Y., Caponi, L., Cazaunau, M., Pangui, E., Journet, E., Nowak, S., Andreae, M. O., Kandler, K., Saeed, T., Piketh, S., Seibert, D., Williams, E., and Doussin, J.-F.: Complex refractive indices and single-scattering albedo of global dust aerosols in the shortwave spectrum and relationship to size and iron content, Atmospheric Chemistry and Physics, 19, 15 503–15 531, https://doi.org/10.5194/acp-19-15503-2019, 2019.

Dick, O., Viallon-Galinier, L., Tuzet, F., Hagenmuller, P., Fructus, M., Reuter, B., Lafaysse, M., and Dumont, M.: Can Saharan dust deposition impact snowpack stability in the French Alps?, The Cryosphere Discussions, pp. 1–32, https://doi.org/10.5194/tc-2022-219, publisher: Copernicus GmbH, 2022.

Dumont, M., Tuzet, F., Gascoin, S., Picard, G., Kutuzov, S., Lafaysse, M., Cluzet, B., Nheili, R., and Painter, T. H.: Accelerated snow melt in the Russian Caucasus mountains after the Saharan dust outbreak in March 2018, Journal of Geophysical Research: Earth Surface, 125, https://doi.org/10.1029/2020JF005641, 2020.

Dumont, M., Gascoin, S., Reveillet, M., Voisin, D., Evrard, O., Gandois, L., Herbin, H., Roux, G. L., and Lefevre, I.: Dataset related to the study "Spatial variability of Saharan dust deposition revealed through a citizen science campaign", https://doi.org/10.5281/zenodo.7969515, 2022.

Evrard, O., Pointurier, F., Onda, Y., Chartin, C., Hubert, A., Lepage, H., Pottin, A.-C., Lefèvre, I., Bonté, P., Laceby, J. P., and Ayrault, S.: Novel Insights into Fukushima Nuclear Accident from Isotopic Evidence of Plutonium Spread along Coastal Rivers, Environmental Science & Technology, 48, 9334–9340, https://doi.org/10.1021/es501890n, 2014.

Evrard, O., Chaboche, P.-A., Ramon, R., Foucher, A., and Laceby, J. P.: A global review of sediment source fingerprinting research incorporating fallout radiocesium (137Cs), Geomorphology, 362, 107 103, https://doi.org/https://doi.org/10.1016/j.geomorph.2020.107103, 2020.

Flanner, M. G., Arnheim, J. B., Cook, J. M., Dang, C., He, C., Huang, X., Singh, D., Skiles, S. M., Whicker, C. A., and Zender, C. S.: SNICAR-ADv3: a community tool for modeling spectral snow albedo, Geoscientific Model Development, 14, 7673–7704, https://doi.org/10.5194/gmd-14-7673-2021, 2021.

Francis, D., Fonseca, R., Nelli, N., Bozkurt, D., Picard, G., and Guan, B.: Atmospheric rivers drive exceptional Saharan dust transport towards Europe, Atmospheric Research, 266, 105 959, https://doi.org/https://doi.org/10.1016/j.atmosres.2021.105959, 2022.

Gascoin, S., Grizonnet, M., Bouchet, M., Salgues, G., and Hagolle, O.: Theia Snow collection: high-resolution operational snow cover maps from Sentinel-2 and Landsat-8 data, Earth System Science Data, 11, 493–514, https://doi.org/10.5194/essd-11-493-2019, 2019.

Ginoux, P.: Warming or cooling dust?, Nature Geoscience, 10, 246–248, https://doi.org/https://doi.org/10.1038/ngeo2923, 2017.

Gourdin, E., Evrard, O., Huon, S., Reyss, J.-L., Ribolzi, O., Bariac, T., Sengtaheuanghoung, O., and Ayrault, S.: Spatial and temporal variability of 7Be and 210Pb wet deposition during four successive monsoon storms in a catchment of northern Laos, Journal of Environmental Radioactivity, 136, 195–205, https://doi.org/https://doi.org/10.1016/j.jenvrad.2014.06.008, 2014.

Greilinger, M. and Kasper-Giebl, A.: Saharan Dust Records and Its Impact in the European Alps, https://doi.org/10.1093/acrefore/9780190228620.013.827, 2021.

Gross, A., Goren, T., Pio, C., Cardoso, J., Tirosh, O., Todd, M. C., Rosenfeld, D., Weiner, T., Custódio, D., and Angert, A.: Variability in Sources and Concentrations of Saharan Dust Phosphorus over the Atlantic Ocean, Environmental Science & Technology Letters, 2, 31–37, https://doi.org/10.1021/ez500399z, 2015.

Hagolle, O., Huc, M., Villa Pascual, D., and Dedieu, G.: A Multi-Temporal and Multi-Spectral Method to Estimate Aerosol Optical Thickness over Land, for the Atmospheric Correction of FormoSat-2, LandSat, VENμS and Sentinel-2 Images, Remote Sensing, 7, 2668–2691, https://doi.org/10.3390/rs70302668, 2015.

Hagolle, O., Huc, M., Desjardins, C., Auer, S., and Richter, R.: MAJA Algorithm Theoretical Basis Document, https://doi.org/10.5281/zenodo.1209633, 2017.

He, C. and He, C.: Modelling light-absorbing particle–snow–radiation interactions and impacts on snow albedo: fundamentals, recent advances and future directions, Environmental Chemistry, https://doi.org/10.1071/EN22013, publisher: CSIRO PUBLISHING, 2022.

Herbin, H., Pujol, O., Hubert, P., and Petitprez, D.: New approach for the determination of aerosol refractive indices – Part I: Theoretical bases and numerical methodology, Journal of Quantitative Spectroscopy and Radiative Transfer, 200, 311–319, https://doi.org/https://doi.org/10.1016/j.jqsrt.2017.03.005, 2017.

Hubert, P., Herbin, H., Visez, N., Pujol, O., and Petitprez, D.: New approach for the determination of aerosol refractive indices – Part II: Experimental set-up and application to amorphous silica particles, Journal of Quantitative Spectroscopy and Radiative Transfer, 200, 320–327, https://doi.org/https://doi.org/10.1016/j.jqsrt.2017.03.037, 2017.

Josse, B., Simon, P., and Peuch, V.-H.: Radon global simulations with the multiscale chemistry and transport model MOCAGE, Tellus B: Chemical and Physical Meteorology, 56, 339–356, 2004.

Kelley, J., Bond, L., and Beasley, T.: Global distribution of Pu isotopes and 237Np, Science of The Total Environment, 237-238, 483–500, https://doi.org/https://doi.org/10.1016/S0048-9697(99)00160-6, 1999.

Le Gall, M., Evrard, O., Foucher, A., Laceby, J. P., Salvador-Blanes, S., Manière, L., Lefèvre, I., Cerdan, O., and Ayrault, S.: Investigating the temporal dynamics of suspended sediment during flood events with 7Be and 210Pbxs measurements in a drained lowland catchment, Scientific Reports, 7, 42 099, https://doi.org/10.1038/srep42099, 2017.

Masson, O., Piga, D., Gurriaran, R., and Amico, D. D.: Impact of an exceptional Saharan dust outbreak in France: PM10 and artificial radionuclides concentrations in air and in dust deposit, Atmospheric Environment, 44, 2478–2486, https://doi.org/https://doi.org/10.1016/j.atmosenv.2010.03.004, 2010.

Meinander, O., Alvarez Piedehierro, A., Kouznetsov, R., Rontu, L., Welti, A., Kaakinen, A., Heikkinen, E., and Laaksonen, A.: Saharan dust transported and deposited in Finland on 23 February 2021, in: EGU General Assembly Conference Abstracts, pp. EGU22–4818, https://doi.org/10.5194/egusphere-egu22-4818.

Mott, R., Vionnet, V., and Grünewald, T.: The seasonal snow cover dynamics: review on wind-driven coupling processes, Frontiers in Earth Science, 6, 197, 2018.

Mărmureanu, L., Marin, C. A., Andrei, S., Antonescu, B., Ene, D., Boldeanu, M., Vasilescu, J., Vițelaru, C., Cadar, O., and Levei, E.: Orange Snow—A Saharan Dust Intrusion over Romania During Winter Conditions, Remote Sensing, 11, https://doi.org/10.3390/rs11212466, 2019.

Nickovic, S., Cvetkovic, B., Petković, S., Amiridis, V., Pejanović, G., Solomos, S., Marinou, E., and Nikolic, J.: Cloud icing by mineral dust and impacts to aviation safety, Scientific reports, 11, 1–9, https://doi.org/https://doi.org/10.1038/s41598-021-85566-y, 2021.

Okin, G. S., Mahowald, N., Chadwick, O. A., and Artaxo, P.: Impact of desert dust on the biogeochemistry of phosphorus in terrestrial ecosystems, Global Biogeochemical Cycles, 18, https://doi.org/https://doi.org/10.1029/2003GB002145, 2004.

Pey, J., Revuelto, J., Moreno, N., Alonso-González, E., Bartolomé, M., Reyes, J., Gascoin, S., and López-Moreno, J. I.: Snow Impurities in the Central Pyrenees: From Their Geochemical and Mineralogical Composition towards Their Impacts on Snow Albedo, Atmosphere, 11, 937, https://doi.org/10.3390/atmos11090937, 2020.

Réveillet, M., Dumont, M., Gascoin, S., Lafaysse, M., Nabat, P., Ribes, A., Nheili, R., Tuzet, F., Ménégoz, M., Morin, S., et al.: Black carbon and dust alter the response of mountain snow cover under climate change, Nature communications, 13, 1–12, 2022.

Rieger, D., Steiner, A., Bachmann, V., Gasch, P., Förstner, J., Deetz, K., Vogel, B., and Vogel, H.: Impact of the 4 April 2014 Saharan dust outbreak on the photovoltaic power generation in Germany, Atmospheric Chemistry and Physics, 17, 13 391–13 415, https://doi.org/10.5194/acp-17-13391-2017, 2017.

Schladitz, A., MüLLER, T., Kaaden, N., Massling, A., Kandler, K., Ebert, M., Weinbruch, S., Deutscher, C., and Wiedensohler, A.: In situ measurements of optical properties at Tinfou (Morocco) during the Saharan Mineral Dust Experiment SAMUM 2006, Tellus B: Chemical and Physical Meteorology, 61, 64–78, https://doi.org/10.1111/j.1600-0889.2008.00397.x, 2009.

Skiles, S. M. and Painter, T. H.: Toward Understanding Direct Absorption and Grain Size Feedbacks by Dust Radiative Forcing in Snow With Coupled Snow Physical and Radiative Transfer Modeling, Water Resources Research, 55, 7362–7378, https://doi.org/10.1029/2018WR024573, 2019.

Skiles, S. M., Flanner, M., Cook, J. M., Dumont, M., and Painter, T. H.: Radiative forcing by light-absorbing particles in snow, Nature Climate Change, 8, 964–971, 2018.

Tobías, A. and Stafoggia, M.: Modeling desert dust exposures in epidemiologic short-term health effects studies, Epidemiology (Cambridge, Mass.), 31, 788, https://doi.org/doi: 10.1097/EDE.0000000000001255, 2020.

Tuzet, F., Dumont, M., Arnaud, L., Voisin, D., Lamare, M., Larue, F., Revuelto, J., and Picard, G.: Influence of light-absorbing particles on snow spectral irradiance profiles, The Cryosphere, 13, 2169–2187, 2019.

UNSCEAR: Effects of Ionizing Radiation, United Nations Scientific Committee on the Effects of Atomic Radiation (UNSCEAR) 2006 Report, Volume I: Report to the General Assembly, Scientific Annexes A and B, United Nations, 2008.

Varga, G.: Changing nature of Saharan dust deposition in the Carpathian Basin (Central Europe): 40 years of identified North African dust events (1979–2018), Environment International, 139, 105 712, https://doi.org/https://doi.org/10.1016/j.envint.2020.105712, 2020.

Varga, G., Dagsson-Waldhauserová, P., Gresina, F., and Helgadottir, A.: Saharan dust and giant quartz particle transport towards Iceland, Scientific reports, 11, 1–12, 2021.

Vernay, M., Lafaysse, M., Monteiro, D., Hagenmuller, P., Nheili, R., Samacoïts, R., Verfaillie, D., and Morin, S.: The S2M meteorological and snow cover reanalysis over the French mountainous areas: description and evaluation (1958–2021), Earth System Science Data, 14, 1707–1733, https://doi.org/10.5194/essd-14-1707-2022, 2022.

Yu, H., Chin, M., Yuan, T., Bian, H., Remer, L. A., Prospero, J. M., Omar, A., Winker, D., Yang, Y., Zhang, Y., Zhang, Z., and Zhao, C.: The fertilizing role of African dust in the Amazon rainforest: A first multiyear assessment based on data from Cloud-Aerosol Lidar and Infrared Pathfinder Satellite Observations, Geophysical Research Letters, 42, 1984–1991, https://doi.org/https://doi.org/10.1002/2015GL063040, 2015.

Appendix: Supplementary material to "Spatial variability of Saharan dust deposition revealed through a citizen

570 **science campaign"**

Supplementary Figures
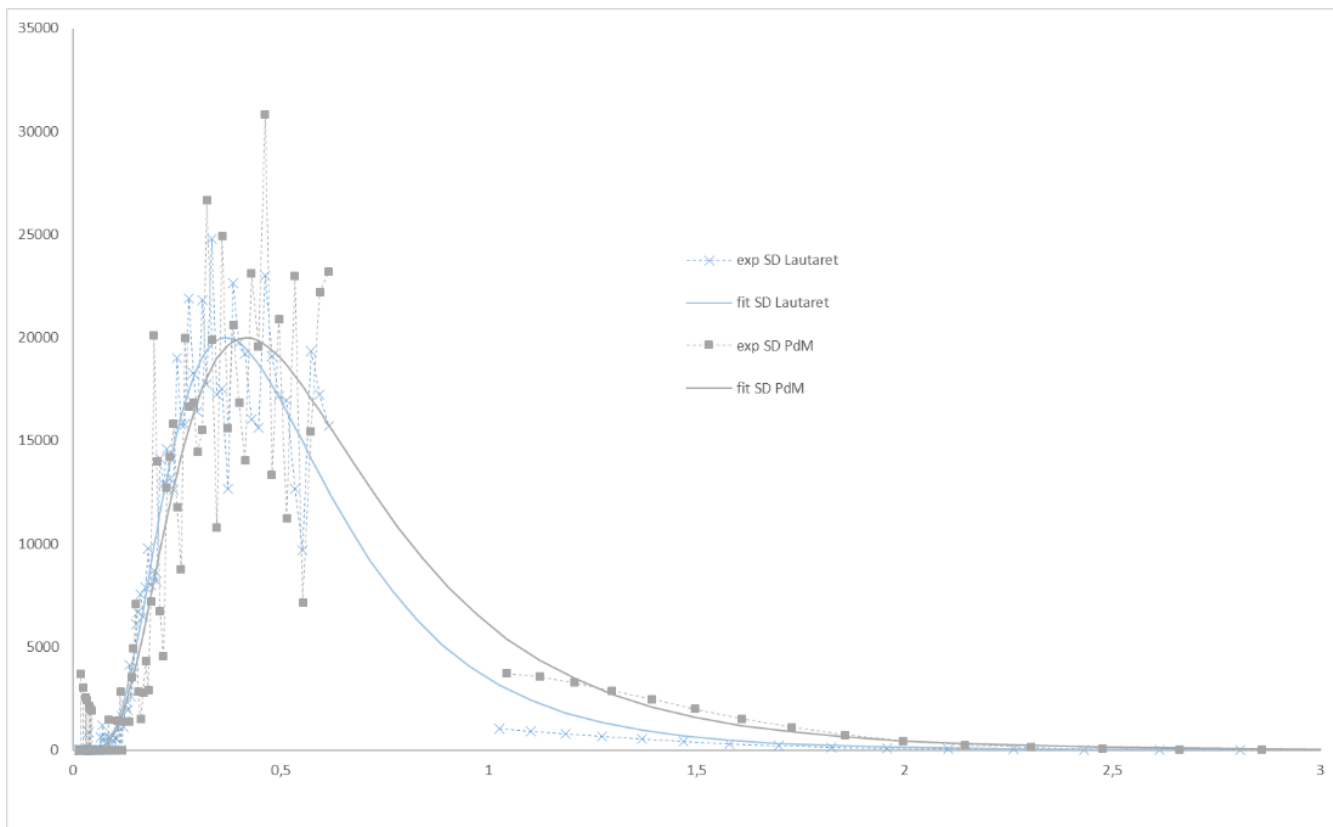
Figure S1. Normalised size distributions of particles from Lautaret (blue) and Pic du Midi (grey), dots : SMPS (0,014—0.6 μm) and the APS (1–20 μm) measurement, full line : Lognormal law.
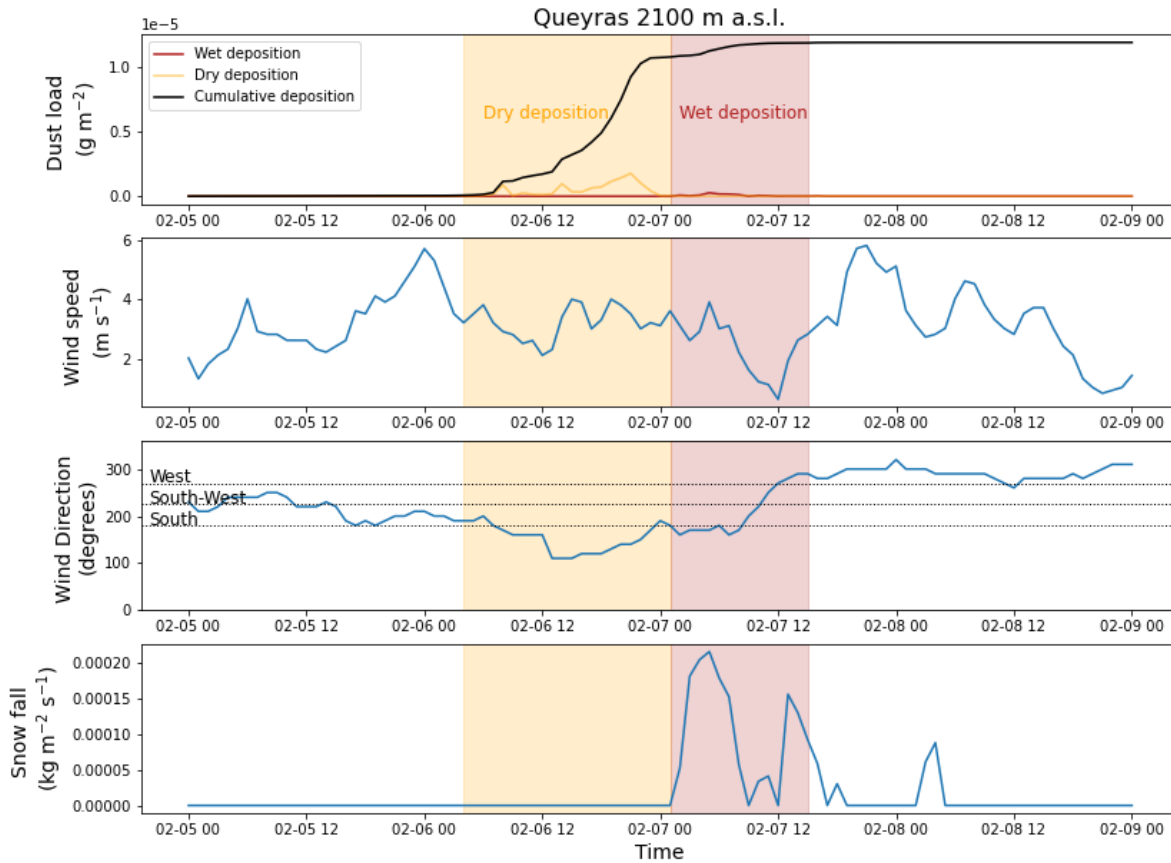
Figure S2. (A) Temporal evolution of the hourly dry (yellow) and wet (red) dust loads during the event at 2100 m a.s.l. in the Queyras Massif. The total cumulative mass deposition is shown by the black line. Depositions are computed based on MOCAGE outputs and corrected according to the observations (i.e. the measured mass of the three closest samples of the site, see Sect. 3.3.1). The dry vs. wet deposition is determined based on SAFRAN precipitation data (see section 2.2). Temporal evolution of the hourly wind speed (B) and direction (C) and the hourly precipitation (D) from SAFRAN reanalysis data. The yellow (red) shaded area represents the dry (wet) deposition of the event, according to SAFRAN precipitation.
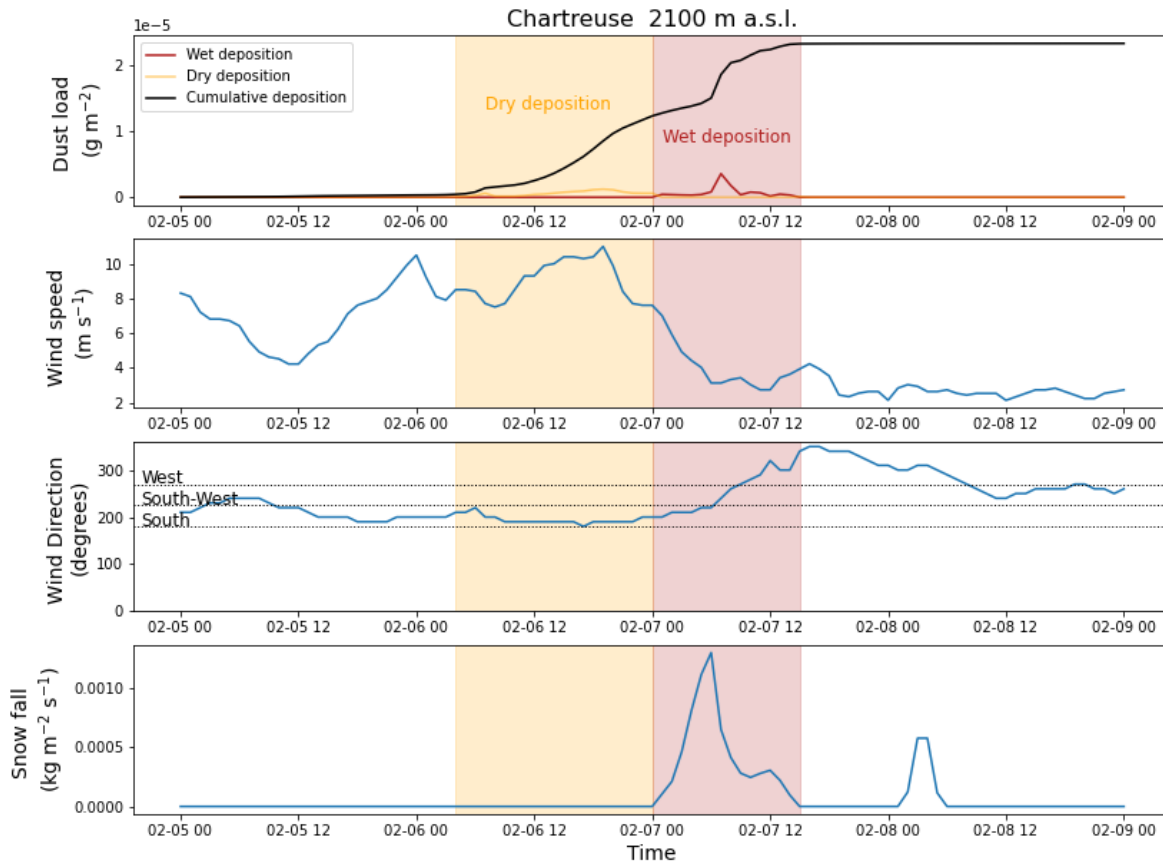
Figure S3. (A) Temporal evolution of the hourly dry (yellow) and wet (red) dust loads during the event at 2100 m a.s.l. in the Chartreuse Massif. The total cumulative mass deposition is shown by the black line. Depositions are computed based on MOCAGE outputs and corrected according to the observations (i.e. the measured mass of the three closest samples of the site, see Sect. 3.3.1). The dry vs. wet deposition is determined based on SAFRAN precipitation data (see section 2.2). Temporal evolution of the hourly wind speed (B) and direction (C) and the hourly precipitation (D) from SAFRAN reanalysis data. The yellow (red) shaded area represents the dry (wet) deposition of the event, according to SAFRAN precipitation.
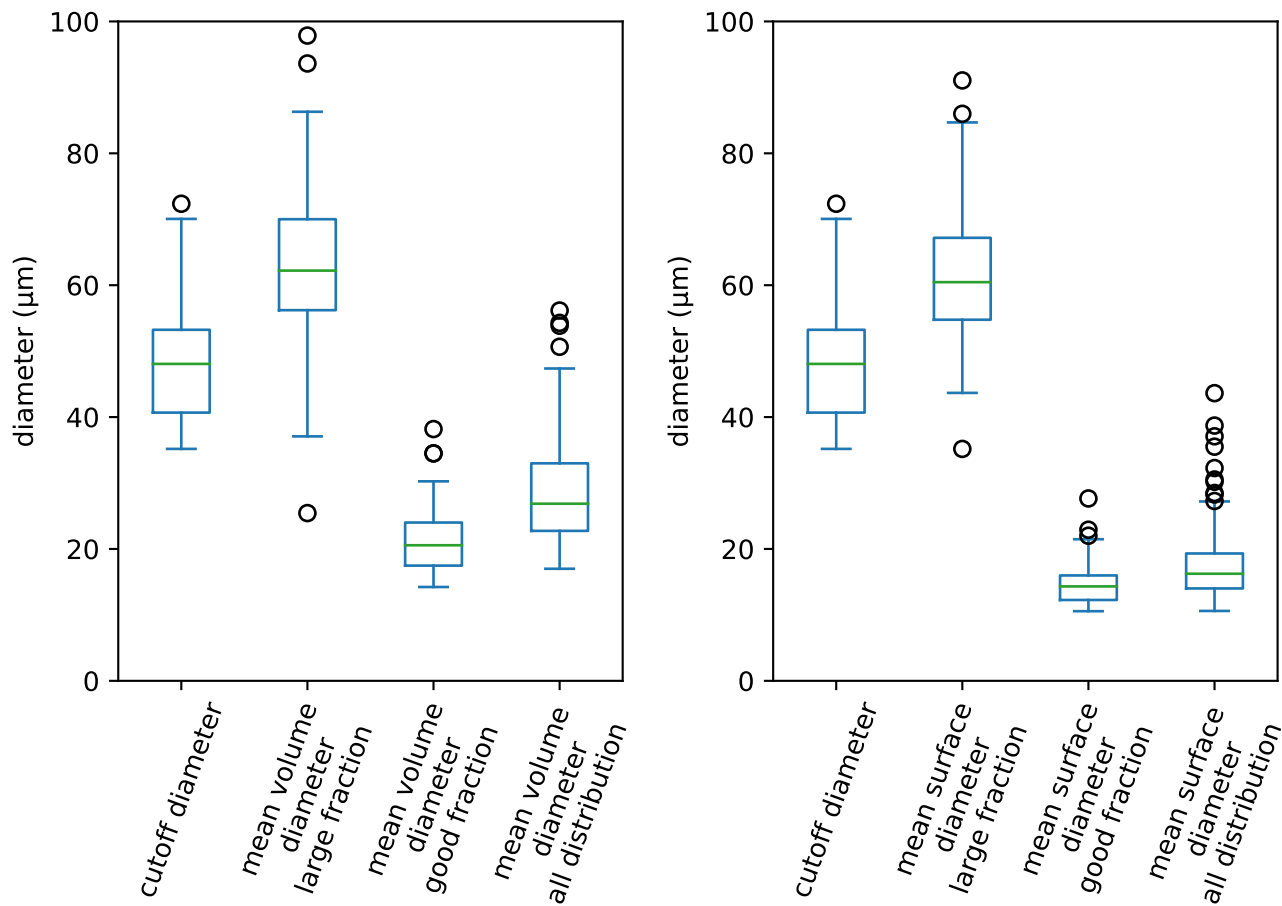
Figure S4. Statistical description of ~~surface~~ volume (left) and ~~volume~~ surface (right) average diameters and how these depend on the cut diameter for the particles with robust statistics. The boxes show the quartiles of the distribution including all samples. Minimum/maximum ranges (excluding outliers) are indicated by the whiskers. Outliers are shown by the circles. The median is shown by the green line.
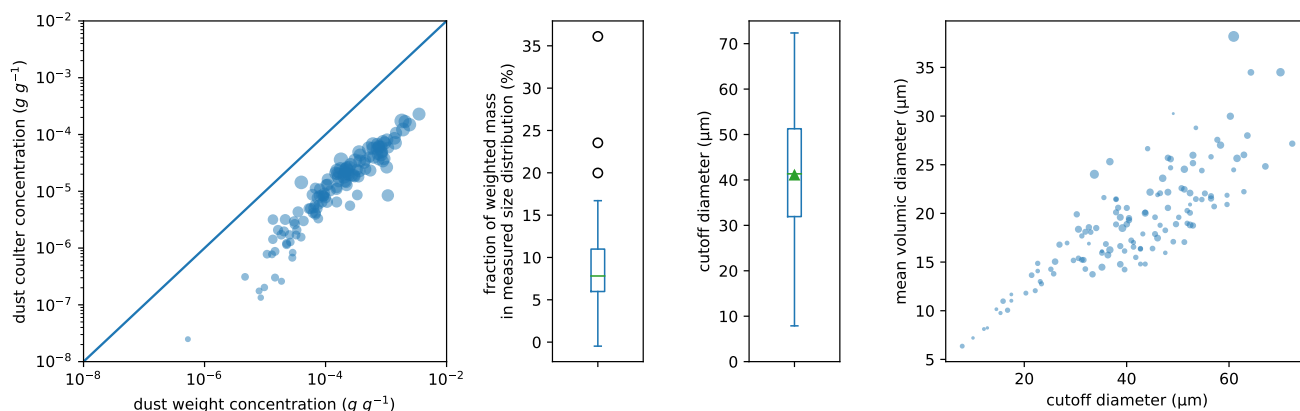
Figure S5. The left panel compares the masses measured on filters and the masses evaluated from the measured size distributions. The middle panels display the distribution of the fraction of the total masses retrieved in the size distribution measurements. The boxes show the quartiles of the distribution including all samples. Minimum/maximum ranges (excluding outliers) are indicated by the whiskers. Outliers are shown by the circles. The median is shown by the green line and the green star. The right panel shows how this fraction depends on both the average diameter of particles and the maximum diameter for statistically robust particle counts. The circle size represents the fraction of weighted mass in measured size distribution

~~Normalised size distributions of particles from Lautaret (blue) and Pic du Midi (grey), dots : SMPS (0,014—0.6 μm) and the APS (1–20 μm) measurement, full line : Lognormal law.~~
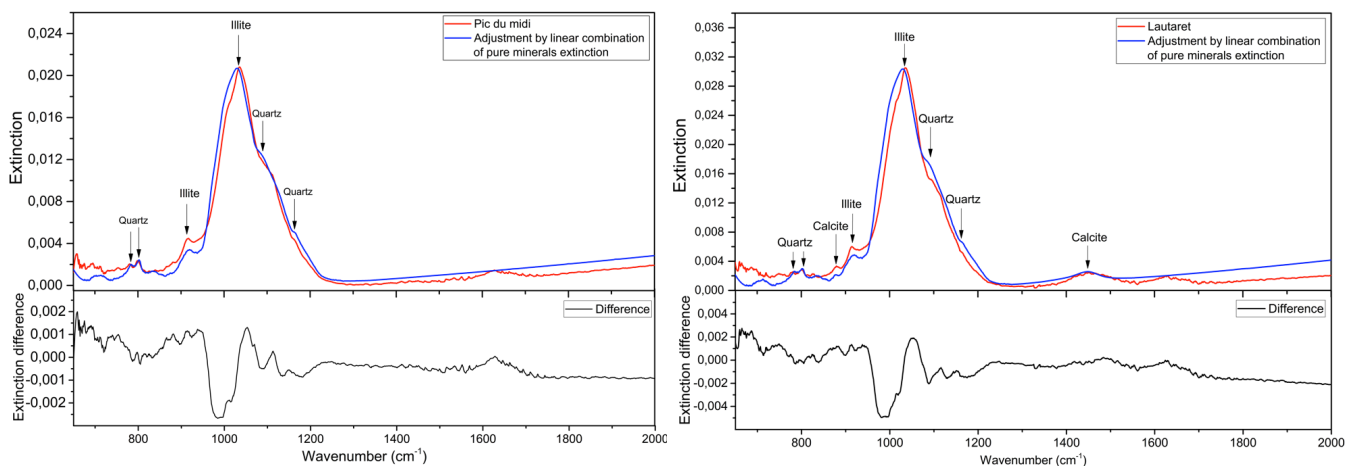
Figure S6. Extinction spectra (red: experimental, blue: simulated using Eq. 2). Left panel: Pic du Midi sample ($C_q = 0.02$, $C_i l = 0.27$, $C_c = 0.007$), right panel: Lautaret sample ($C_q = 0.03$, $C_i l = 0.53$).
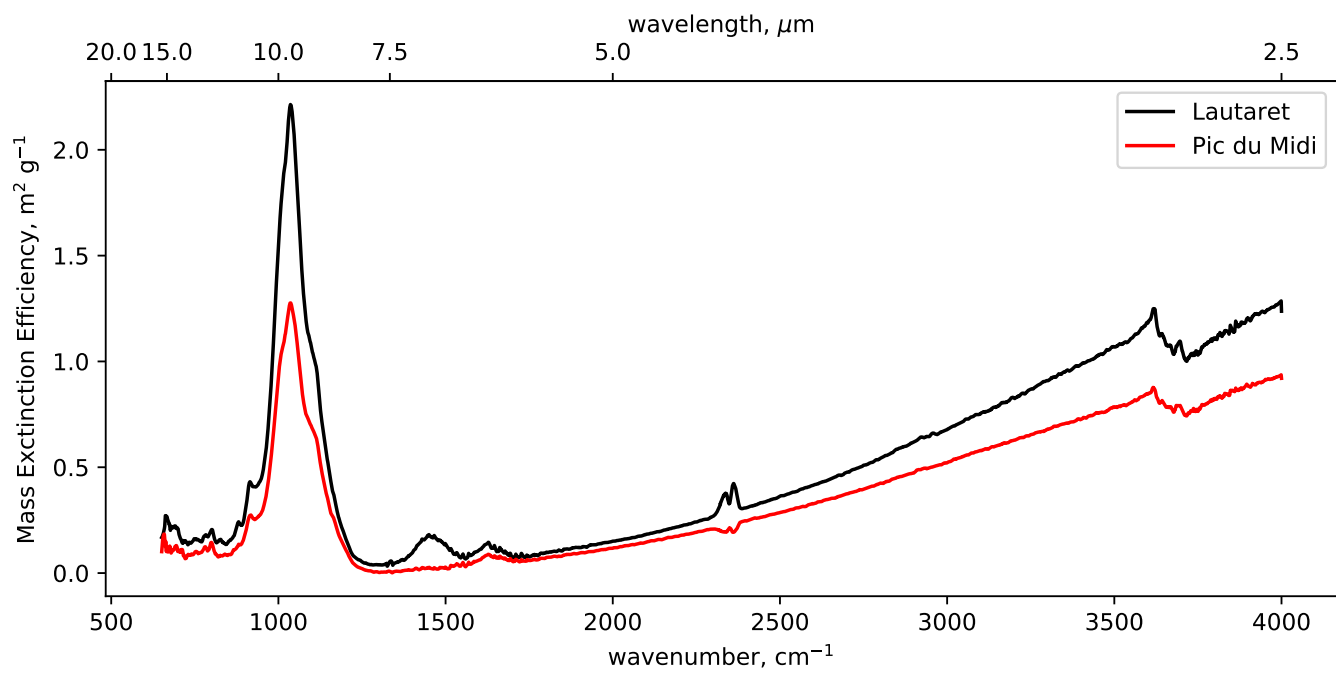
Figure S7. Mass extinction efficiency in m^2 g^{-1} for Lautaret et Pic du Midi samples.